The Astrophysical Journal, 837:55 (18pp), 2017 March 1 https://doi.org/10.3847/1538-4357/aa5d12
© 2017. The American Astronomical Society. All rights reserved.

Recovering Interstellar Gas Properties with HI Spectral Lines: A Comparison between Synthetic Spectra and 21-SPONGE

Claire E. Murray[1], Snežana Stanimirović[1], Chang-Goo Kim[2], Eve C. Ostriker[2], Robert R. Lindner[1], Carl Heiles[3], John M. Dickey[4], and Brian Babler[1]
[1] Department of Astronomy, University of Wisconsin, Madison, WI 53706, USA; cmurray@astro.wisc.edu
[2] Department of Astrophysical Sciences, Princeton University, Princeton, NJ 08544, USA
[3] Radio Astronomy Lab, UC Berkeley, 601 Campbell Hall, Berkeley CA 94720, USA
[4] University of Tasmania, School of Maths and Physics, Hobart, TAS 7001, Australia
Received 2016 December 6; revised 2017 January 16; accepted 2017 January 27; published 2017 March 2

Abstract

We analyze synthetic neutral hydrogen (H I) absorption and emission spectral lines from a high-resolution, three-dimensional hydrodynamical simulation to quantify how well observational methods recover the physical properties of interstellar gas. We present a new method for uniformly decomposing H I spectral lines and estimating the properties of associated gas using the Autonomous Gaussian Decomposition (AGD) algorithm. We find that H I spectral lines recover physical structures in the simulation with excellent completeness at high Galactic latitude, and this completeness declines with decreasing latitude due to strong velocity-blending of spectral lines. The temperature and column density inferred from our decomposition and radiative transfer method agree with the simulated values within a factor of <2 for the majority of gas structures. We next compare synthetic spectra with observations from the 21-SPONGE survey at the Karl G. Jansky Very Large Array using AGD. We find more components per line of sight in 21-SPONGE than in synthetic spectra, which reflects insufficient simulated gas scale heights and the limitations of local box simulations. In addition, we find a significant population of low-optical depth, broad absorption components in the synthetic data which are not seen in 21-SPONGE. This population is not obvious in integrated or per-channel diagnostics, and reflects the benefit of studying velocity-resolved components. The discrepant components correspond to the highest spin temperatures ($1000 < T_s < 4000$ K), which are not seen in 21-SPONGE despite sufficient observational sensitivity. We demonstrate that our analysis method is a powerful tool for diagnosing neutral interstellar medium conditions, and future work is needed to improve observational statistics and implementation of simulated physics.

Key words: ISM: clouds – ISM: structure – radio lines: ISM

1. Introduction

Neutral hydrogen (H I) in the interstellar medium (ISM) plays a crucial role in the life cycles of galaxies. The atomic medium provides the main fuel reservoir for molecular gas and, ultimately, star formation. Furthermore, the structure of interstellar H I bears important clues to the nature of gas recycling via radiative and dynamical feedback and Galactic winds (e.g., McClure-Griffiths et al. 2013).

Throughout the ISM, H I exists in a "multi-phase" state, characterized by two thermally stable phases in pressure equilibrium (Field et al. 1969; McKee & Ostriker 1977; Wolfire et al. 2003): the cold neutral medium (CNM) and warm neutral medium (WNM). An effective constraining observable for the balance between the CNM and WNM is the excitation temperature (a.k.a., spin temperature, T_s) of the gas. However, both emission and absorption by the 21 cm hyperfine transition of H I are required to measure T_s. Therefore, although the CNM ($T_s \sim 20$–200 K) has been extensively analyzed with H I absorption (e.g., Crovisier et al. 1978; Dickey et al. 2003; Heiles & Troland 2003a), excellent sensitivity is required to constrain the temperature of the WNM ($T_s \sim 1000$–7000 K), and few measurements exist (Carilli et al. 1998; Dwarakanath et al. 2002; Roy et al. 2013; Murray et al. 2014, 2015).

Furthermore, to understand the physical mechanisms responsible for observed H I properties, comparisons between observations and theory are necessary. Synthetic data sets from numerical simulations provide a means to: (1) assess the power of observational diagnostics to reveal the inherent state of astronomical systems, and (2) test whether complex simulations recover all the properties of real systems. For example, the velocity structures of synthetic spectral lines provide important diagnostics of interstellar turbulence (e.g., Falgarone et al. 1994), and the nature of CNM dynamics (Hennebelle et al. 2007; Saury et al. 2014). Furthermore, synthetic observations have been used extensively to investigate molecule formation (Shetty et al. 2011; Smith et al. 2014; Duarte-Cabral et al. 2015; Duarte-Cabral & Dobbs 2016) and Galactic morphology (Douglas et al. 2010; Acreman et al. 2012; Pettitt et al. 2014). Important observational biases can be directly quantified using these comparisons. For example, considering correspondence between the true positions and observed velocities of molecular clouds, Beaumont et al. (2013) showed that the superposition of clouds along the line of sight (LOS) introduces significant uncertainty to observational estimates of cloud mass, size, and velocity dispersion.

However, numerical simulations with suitable dynamic range and resolution for describing the dynamics of both the CNM and WNM have only recently been performed. Kim et al. (2014) constructed a sample of synthetic H I absorption and emission spectral lines from their three-dimensional (3D) hydrodynamical simulations (Kim et al. 2013). Comparing conditions in the simulated data with properties inferred from synthetic spectra, Kim et al. (2014) found excellent agreement between "true" and "observed" per-channel and

LOS-integrated properties such as column density and spin temperature. Furthermore, they showed that column densities computed in the optically thin limit significantly underestimate the true column density when the H I optical depth is greater than $\tau \sim 1$. This agrees with previous comparisons of observed and simulated LOS column density by Chengalur et al. (2013), who used Monte Carlo simulated spectra to test the role of optically thick H I. However, Kim et al. (2014) found the discrepancy factor to be much smaller than Chengalur et al. (2013), indicating that when proper dynamics are considered, spectral line blending due to overlapping cold clouds is not significant.

Although LOS-integrated ISM properties provide important diagnostics, interpretation is more complicated for multi-temperature, as opposed to isothermal, conditions. Observations show that even high Galactic latitude LOSs contain several components of varying spin temperature (e.g., Heiles & Troland 2003a; Begum et al. 2010; Roy et al. 2013; Murray et al. 2015). The technique of Gaussian decomposition is one method that can identify individual spectral components from disparate H I phases, and has been used extensively to disentangle complex spectral lines (e.g., Lazareff 1975; Mebold et al. 1982; Dickey & Lockman 1990; Mohan et al. 2004). When applied to both H I absorption and emission spectra, Gaussian decomposition can be used to estimate the spin temperatures of individual spectral features and the fraction of CNM along the LOS (Heiles & Troland 2003a; Stanimirović et al. 2014; Murray et al. 2015). However, the method suffers from non-uniqueness complications, as Gaussian functions do not form an orthogonal basis (e.g., Heiles & Troland 2003a) and the number of Gaussian functions used to produce reasonable spectral fits can vary significantly. For example, comparing the Gaussian decompositions of the Galactic H I absorption spectrum toward 3C138, there are no fitted components which agree between the six found by Murray et al. (2015) and the 13 found by Roy et al. (2013). Furthermore, no quantitative estimates of how well Gaussian functions recover the properties of interstellar gas exist.

One of the major scientific goals for future H I observations with the Australian Square Kilometer Array Pathfinder (ASKAP) and the Square Kilometer Array will be to understand the temperature distribution of the ISM and how it relates to the life cycles of galaxies using thousands of spectra (e.g., Dickey et al. 2013; McClure-Griffiths et al. 2015). However, the first step in this undertaking is to understand the biases and limitations of our observational and analysis methods in reproducing interstellar gas properties. This is best done by analyzing synthetic H I data from numerical simulations, which include realistic physical processes, and also provide full 3D information on simulated H I structures (e.g., density, temperature, velocity).

Accordingly, we begin this paper by quantifying how well Gaussian analysis of H I spectral lines via simple radiative transfer recovers "true" interstellar gas properties by analyzing synthetic 21 cm spectral profiles derived from 3D hydrodynamical simulations from Kim et al. (2013, 2014). To analyze the synthetic spectral profiles, we use the Autonomous Gaussian Decomposition (AGD) algorithm (Lindner et al. 2015). AGD implements derivative-based computer vision to perform Gaussian decomposition of spectral lines, enabling efficient, reproducible, and objective spectral decomposition.

In the second half of the paper, we compare synthetic and observed H I spectra objectively using the same methodology. For this we use data from the 21 cm Spectral Line Observations of Neutral Gas with the Very Large Array (VLA) (21-SPONGE) survey, one of the most sensitive Galactic 21 cm surveys (Murray et al. 2015), as well as the Kim et al. synthetic H I spectra. We assess the ways in which the detailed statistical properties of synthetic spectra may agree or disagree with the statistics of observed spectra. This in turn reflects the influence of the star formation feedback mechanisms and other physics of the simulations. We especially focus on the importance of Lyα resonant scattering for H I excitation and the temperature distribution.

In Section 2, we describe the 21-SPONGE observations, and in Section 3 we describe Kim et al. simulations and synthetic data. We present and discuss our analysis method in Section 4. In Section 5, we compare the properties inferred from synthetic spectra with the simulated properties of gas along the same LOS. We then compare the synthetic spectra with 21-SPONGE observations in Section 6. Finally, we present our summary and conclusions in Section 7.

2. Observations

For observations of Galactic H I, we use data from the 21-SPONGE survey (Murray et al. 2015). 21-SPONGE is the most sensitive survey of Galactic H I absorption at the Karl G. Jansky Very Large Array (VLA) to date. We target strong extragalactic radio continuum sources mostly at high Galactic latitudes ($|b| > 5°$), and consistently reach rms noise in H I optical depth of $\sigma_\tau < 10^{-3}$ per 0.4 km s^{-1} channels.

21-SPONGE utilizes H I emission observations along the same LOS from the Arecibo Observatory ($\sim$3.′5 beam at 21 cm). The emission spectrum in the direction of each source is computed by observing a pattern of 16 off-source positions and interpolating across the target position (see, e.g., Heiles & Troland 2003a, hereafter HT03). We note that the Arecibo H I emission profiles are not corrected for an effect known as "stray radiation," wherein radiation enters the main telescope beam through higher-order side lobes. Although stray radiation can be modeled and removed from H I emission data (e.g., Leiden Argentine Bonn (LAB) and GASS surveys; Kalberla et al. 2005; McClure-Griffiths et al. 2009; Kalberla et al. 2010), it is a complex process requiring stable beam shapes which are not achieved at Arecibo. Comparison between the GALFA-H I survey at Arecibo and the stray radiation-corrected LAB survey suggested that stray radiation likely does not contribute more than $\sim$500 mK over $\sim$50 km s^{-1} to observed H I brightness temperature (Peek et al. 2011). We emphasize that the effect is only significant for emission, not absorption.

Armed with high-sensitivity H I absorption and emission spectra along each LOS, 21-SPONGE is sensitive to H I column densities and temperatures from all neutral ISM phases, including the CNM, WNM, and thermally unstable medium.

In Murray et al. (2015), we presented the survey design, analysis methods, and initial results for 21-SPONGE. To derive physical properties of interstellar gas along each LOS, we decomposed (by hand) H I absorption and emission spectral pairs simultaneously into Gaussian functions, and solved radiative transfer equations to derive the column density and spin temperature of individual spectral components, taking into account the presence of self-absorption and the order of

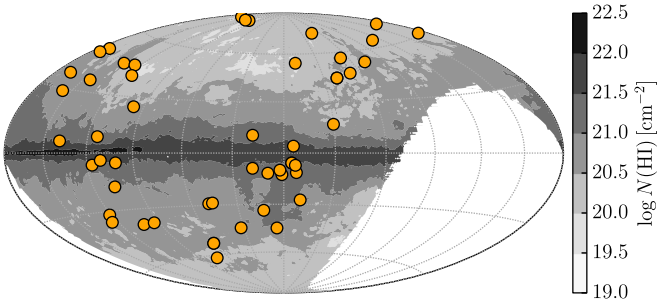

Figure 1. Galactic H I column density (N(H I)) map from the Leiden Dwingeloo Survey (Hartmann & Burton 1997). The locations of the 52 21-SPONGE H I absorption line sources (orange circles) are overlaid.

features along each LOS (as done, e.g., in HT03, Stanimirović & Heiles 2005; Stanimirović et al. 2014). We found excellent agreement with previous H I absorption surveys. The high sensitivity of 21-SPONGE allowed us to extend the maximum H I spin temperatures detected directly in absorption and emission from 600 K in HT03 to ∼1500 K (Murray et al. 2015).

Figure 1 displays the positions of the 52 21-SPONGE sources overlaid on an H I column density map from the Leiden Dwingeloo Survey (Hartmann & Burton 1997). The targets probe a large range in Galactic latitude.

3. Numerical Simulations

We analyze recent high-resolution Galactic ISM simulations by Kim et al. (2013, hereafter KOK13). These simulations include momentum feedback from supernovae, time-varying heating, interstellar cooling appropriate for warm/cold gas, galactic differential rotation, gaseous self-gravity, and external gravity from dark matter and stars. We refer the reader to KOK13 for a full description of the numerical setup and methods.

Using these simulations, Kim et al. (2014, hereafter KOK14) constructed a set of synthetic spectral lines sampling the local ISM. Assuming an observer sits in the center of the simulation, they selected 10^4 positions randomly distributed in Galactic latitude (l) and longitude (b) and extracted the number density (n), temperature (kinetic, T_k, and spin, T_s), and velocity (v) as functions of path length (s). These LOSs are restricted to $|b| > 4.^\circ9$ and $s \leqslant 3$ kpc so that the limited horizontal extent of the simulation does not adversely affect the results, as would be a concern at low Galactic latitude. For the particular KOK13 simulation we analyze in this work (the model denoted "QA10"), galactic rotation was applied with assumed angular velocity of $\Omega = 28\,\mathrm{km\,s^{-1}}$ and gas surface density $\Sigma = 10\ M_\odot\ \mathrm{pc}^{-2}$ (KOK13).

For each observed LOS, KOK14 produced synthetic H I 21 cm emission and absorption as functions of radial velocity using analytical radiative transfer and a simple prescription for line excitation. The reader is referred to Section 2.3 of KOK14 for a complete description of the methods used to construct the synthetic spectra.

In particular, as part of their model for synthetic 21 cm level populations, KOK14 considered indirect radiative transitions due to resonant scattering by Lyα photons (the Wouthuysen–Field (WF) effect; Wouthuysen 1952; Field 1959) in addition to collisions and direct radiative transitions. They parameterized the WF effect following Field (1959) with a constant value for the Galactic Lyα photon number density, n_α, inferred from Liszt (2001) to be $n_\alpha = 10^{-6}\,\mathrm{cm}^{-3}$. This value of n_α is highly uncertain and difficult to constrain observationally or numerically. Given that observed LOS-integrated and per-channel properties are dominated by high-optical depth gas, wherein the 21 cm transition is already thermalized by collisions due to high densities, the WF effect does not significantly affect these values. The WF effect should be most important for the WNM, where generally $T_s \leqslant T_k$ due to the inefficiency of collisions at thermalizing the 21 cm transition (e.g., Liszt 2001). Indeed, at high T_s the WF effect is significant (c.f., Figures 9(a), 10(a) of KOK14).

We note that the KOK13 simulations do not include chemistry and the H I-to-H_2 conversion. In addition, their implemented supernova feedback injects momentum and not thermal energy, resulting in the absence of a hot ($T \sim 10^5$–10^7 K) medium. Although for the warm and cold medium these are secondary effects, and they are being addressed in ongoing simulations with thermal supernova feedback to create a hot ISM (Kim & Ostriker 2016), we need to keep these limitations in mind when considering properties of synthetic spectra from KOK14.

In this paper, we analyze components within the synthetic KOK14 H I spectral pairs to investigate how radiative transfer-based Gaussian fitting reproduces real physical quantities. From their catalog of 10^4 spectral pairs, we selected those without saturated (defined here as $\tau \geqslant 3$) or NaN-valued absorption lines, for a final catalog of 9355 H I spectral pairs. To simulate observational conditions, we added Gaussian-distributed noise with an amplitude of $\sigma_\tau = 10^{-3}$ to each absorption spectrum (equal to the median rms noise in τ per channel from 21-SPONGE) and $\sigma_{T_B} = 0.2$ K to each emission spectrum (equal to the median rms noise in T_B per channel in 21-SPONGE).

4. Gaussian Decomposition with AGD

To perform Gaussian fits to H I spectra (either real or synthetic), we use the AGD algorithm (Lindner et al. 2015). AGD implements derivative spectroscopy and machine learning techniques to efficiently and objectively provide initial guesses (i.e., amplitude, width, mean velocity) for multiple-Gaussian fits to spectral line data.

Before implementing AGD, we trained the algorithm to maximize the decomposition accuracy. We began by constructing a synthetic H I data set from the Gaussian components detected by the Millennium Arecibo 21 cm Absorption Line Survey (HT03, Heiles & Troland 2003b). The synthetic training data set construction and training are described fully in Lindner et al. (2015), and summarized here for clarity. We selected the number of components in each synthetic spectrum to be a uniform random integer ranging from the mean number of components in the survey (3) to the maximum number (8; HT03), and then drew the component parameters from the published HT03 amplitude, full width at half maximum (FWHM), and mean velocity distributions with replacement. As done with the KOK14 synthetic spectra, we added Gaussian-distributed noise with an amplitude of $\sigma_\tau = 10^{-3}$ to each absorption spectrum (equal to the median rms noise in τ per channel from 21-SPONGE) and $\sigma_{T_B} = 0.2$ K to each emission spectrum (equal to the median rms noise in T_B per channel in 21-SPONGE). The synthetic training sets for absorption and emission consist of 20 spectra each.

After constructing the synthetic training data set, we used the Python implementation of AGD, GaussPy, to decompose the

Table 1
AGD Summary

Source	LOS (number)	Absorption (N_{AGD})		Emission (N_{AGD})		Matched[a]	
		(total)	(per LOS)[b]	(total)	(per LOS)[b]	(total)	(per LOS)[b]
KOK14	9355	14023	1.5 ± 1.7	23475	2.5 ± 1.4	9218	1.0 ± 1.1
KOK14 (no WF)	9355	15468	1.7 ± 1.8	23519	2.5 ± 1.4	9490	1.0 ± 1.1
21-SPONGE	52	237	4.6 ± 3.0	326	6.3 ± 2.9	88	1.7 ± 1.3

Notes.
[a] "Matched" statistics will be discussed in Section 6.
[b] Mean and standard deviation over all LOSs.

synthetic training data set for different values of the "two-phase" smoothing parameters α_1 and α_2. These smoothing parameters serve to identify the types of spectral properties present in the data. Beginning with initial choices for α_1 and α_2 and a signal-to-noise ratio (S/N) threshold below which the algorithm will not select components (S/N = 3.0), GaussPy computes the accuracy of the decomposition (i.e., how closely the derived model parameters are to the true model parameters), for iteratively different values of α_1 and α_2 until it converges on minimal model residuals and maximum decomposition accuracy. After training, we found accuracies of 80% and 70% for H I absorption and emission decompositions, respectively. The resulting values are $\alpha_1 = 1.12$ and $\alpha_2 = 2.73$ for absorption and $\alpha_1 = 1.70$ and $\alpha_2 = 3.75$ for emission.

With trained values of α_1 and α_2 in hand, we used GaussPy to apply the AGD algorithm identically (i.e., same values of α_1, α_2, and S/N) to the observed 21-SPONGE and simulated KOK14 spectra to derive lists of Gaussian parameters for each data set. Table 1 summarizes the decomposition results for the emission and absorption spectra from 21-SPONGE and KOK14 including the WF effect and without the WF effect ("no WF"). The typical uncertainties in the fitted parameters are ∼1%–10% from the least-squares fit applied by AGD.

5. Assessing the Power of the Gaussian-fitting Method with Synthetic H I Spectra

From the KOK14 simulations, we have information about the density and spin temperature as a function of distance ($n(s)$, $T_s(s)$), as well as the optical depth and brightness temperature as a function of velocity ($\tau(v)$, $T_B(v)$) for each LOS. Therefore, following AGD analysis, we can compare inferred properties from spectral lines to the true gas properties within the simulated ISM. This will allow us to quantify the biases and limitations of Gaussian analysis in reproducing realistic physical properties.

5.1. Defining Gas Structures in Position and Velocity

Given that $\tau \propto n/T_s$, we define simulated gas structures by selecting peaks in n/T_s along each LOS. To select a threshold value, we consider the parameters of the simulated ISM from KOK13. The gas temperature and density PDFs in their Figure 8 display strong bi-modality indicative of multiple H I phases. The ratio n/T_s is high for the CNM and low for the WNM. In identifying gas "structures" along the LOS, we wish to mark concentrations using CNM-like peaks. We select $n \sim 2\ \mathrm{cm^{-3}}$ and $T \sim 10^3\ \mathrm{K}$ as representative values between the peaks of the published bi-modal PDFs (KOK13). These values correspond to a threshold of $(n/T_s)_{\mathrm{thresh}} = 0.002\ \mathrm{cm^{-3}\ K^{-1}}$. We experimented with different values of this threshold, and the subsequent results do not change significantly.

In Figure 2, we display $(n/T_s)(s)$ (left), $\tau(v)$ (middle), and $T_B(v)$ (right) for five example LOSs from KOK14. The positions of peaks above $(n/T_s)_{\mathrm{thresh}} = 0.002\ \mathrm{cm^{-3}\ K^{-1}}$ ("structures") are plotted as colored circles. Across all 9355 synthetic LOSs, there are 7582 structures with $(n/T_s) > 0.002\ \mathrm{cm^{-3}\ K^{-1}}$.

To compare the properties of simulated gas structures with synthetic spectral lines, we first determine the position and velocity range (i.e., line width) of each physical gas structure. We estimate the velocity of each gas structure, v_{sim}, by computing the average velocity ($v(s)$) of channels spanned by each peak in n/T_s weighted by their densities ($n(s)$), specifically,

$$v_{\mathrm{sim}} = \frac{\int_{\mathrm{structure}} n(s)\, v(s)\, ds}{\int_{\mathrm{structure}} n(s)\, ds}, \quad (1)$$

where "structure" refers to all pixels spanned by each peak above $(n/T_s)_{\mathrm{thresh}} = 0.002\ \mathrm{cm^{-3}\ K^{-1}}$. These values are plotted in the middle and right columns of Figure 2 as circles with colors corresponding to the labels in the left column (n/T_s). Next, we estimate the FWHM of the structure based on its thermal and turbulent properties. We compute the inferred thermal line width, $\Delta v_{\mathrm{therm}}$, by solving (e.g., Equation (9.31), Draine 2011),

$$\Delta v_{\mathrm{therm}} = 2.15 \sqrt{\frac{T_{\mathrm{mean}}/100\ \mathrm{K}}{M/m_{\mathrm{H}}}} = 0.190 \sqrt{T_{\mathrm{mean}}}\ \mathrm{km\ s^{-1}} \quad (2)$$

where we assume $M = \mu m_{\mathrm{H}}$ for mean molecular weight $\mu = 1.27$ (c.f., KOK13), and T_{mean} is the harmonic mean kinetic temperature of the gas spanned by each peak, given by

$$T_{\mathrm{mean}} = \frac{\int_{\mathrm{structure}} n(s)\, ds}{\int_{\mathrm{structure}} (n/T)(s)\, ds}. \quad (3)$$

We then estimate the contribution from turbulent line broadening, Δv_{turb}, by computing the standard deviation of the velocities spanned by each structure, multiplied by a factor of 2.355 to convert to an FWHM, or

$$\Delta v_{\mathrm{turb}} = 2.355 \sqrt{\frac{\int_{\mathrm{structure}} n(s)\, (v(s) - v_{\mathrm{sim}})^2\, ds}{\int_{\mathrm{structure}} n(s)\, ds}}. \quad (4)$$

The final estimate of the velocity FWHM of each structure, Δv_{sim}, is a quadratic sum of the thermal and

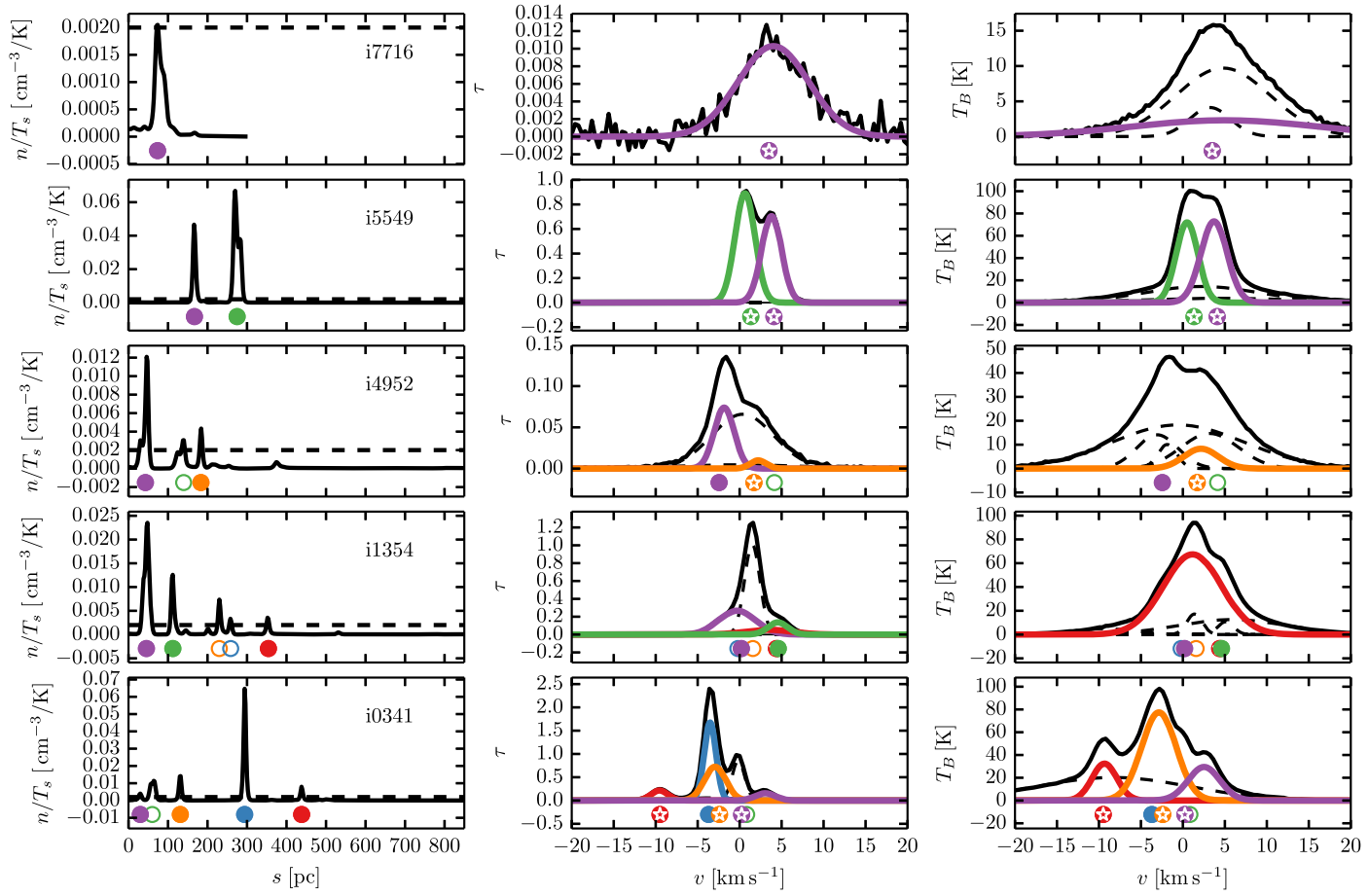

Figure 2. Example LOSs from KOK14. Left: density over spin temperature (n/T_s) as a function of distance (s) along the LOS. Middle: synthetic optical depth as a function of velocity ($\tau(v)$). Right: synthetic brightness temperature as a function of velocity ($T_B(v)$). Gas structures defined by peaks above $(n/T_s)_{\rm thresh} = 0.002\,{\rm cm^{-3}\,K^{-1}}$ (dashed line, left column) are indicated by colored circles in each panel. If a structure from the left column matches with an AGD absorption component in the middle column according to Equations (6) and (8), the circles are filled and the matching AGD component is plotted in the corresponding color (unmatched components are plotted in dashed lines). If a structure matches with an AGD absorption *and* emission component according to Equations (9) and (10), the circle symbol has a white star within it.

turbulent contributions (Equations (2) and (4)), or $\Delta v_{\rm sim} = \sqrt{\Delta v_{\rm therm}^2 + \Delta v_{\rm turb}^2}$, and has values between ~1–10 km s^{-1} for a range of density threshold choices.

5.2. Matching Gas Structures with H I Absorption Lines

To match AGD-fitted Gaussian absorption lines with gas structures along each LOS, we use two matching criteria. First, we define δ_v to be the difference in mean velocity of a Gaussian component fitted by AGD in absorption (v_0) with the estimated velocity of the gas structure ($v_{\rm sim}$) in terms of the measured FWHM from the AGD fit (Δv_0), or

$$\delta_v \equiv \frac{|v_0 - v_{\rm sim}|}{\Delta v_0/2.355}. \quad (5)$$

For a gas structure to match a Gaussian component, we require that their positions in velocity be less than one standard deviation away from each other, so that

$$\delta_v \leqslant 1. \quad (6)$$

Second, we define $R_{\rm FWHM}$ to be the ratio of the FWHM of a component in absorption (Δv_0) and the estimated FWHM of the gas structure in velocity ($\Delta v_{\rm sim}$), or

$$R_{\rm FWHM} \equiv \Delta v_{\rm sim}/\Delta v_0. \quad (7)$$

For a structure to match a Gaussian component, we require that the structure's simulated velocity FWHM ($\Delta v_{\rm sim}$), including the thermal and turbulent contributions, be similar to the FWHM of the Gaussian component (within a factor of 3), or

$$0.3 \leqslant R_{\rm FWHM} \leqslant 3. \quad (8)$$

We note that choices of cutoff values for $R_{\rm FWHM}$ does not significantly change the results, as the criterion described by Equation (6) dominates the matching. In addition, we emphasize that the matching criteria were designed to be as simple as possible to minimize imposed selection biases.

In Figure 2, the circle markers for structures which match with AGD absorption components according to Equations (6) and (8) are filled, and the matching AGD absorption component is plotted in the corresponding color in the middle panel. If a structure does not have an AGD match, the circle marker is unfilled. Of the 7582 total structures, there are 6097 structures with matches to AGD absorption components.

5.2.1. Matching H I Absorption Lines with H I Emission Lines

Both H I absorption ($\tau(v)$) and emission ($T_B(v)$) information are required to constrain the spin temperature (T_s) and column density (N(H I)) of neutral gas in the ISM via radiative transfer. Therefore, to compare the density and temperature of simulated gas structures with properties inferred from observations, we need to determine the optical depth *and* brightness temperature of each structure.

To match H I absorption lines with H I emission lines fitted by AGD, we apply a similar set of match criteria as described by Equations (6) and (8). Specifically,

$$\delta_{v,\mathrm{AGD}} \equiv \frac{|v_0 - v_{0,\mathrm{em}}|}{\Delta v_0/2.355} \leqslant 1, \tag{9}$$

$$1 \leqslant R_{\mathrm{FWHM,AGD}} \equiv \Delta v_{0,\mathrm{em}}/\Delta v_0 \leqslant 3, \tag{10}$$

where ($v_{0,\mathrm{em}}$, $\Delta v_{0,\mathrm{em}}$) are the mean velocity and FWHM of an AGD component fitted to $T_B(v)$. We impose the requirement that $R_{\mathrm{FWHM,AGD}} \geqslant 1$ to ensure that the matched line width is larger in emission than absorption, and impose $R_{\mathrm{FWHM,AGD}} \leqslant 3$ in order to ensure that the line widths are reasonably similar. We do not include a criterion for matching component amplitudes here, because the amplitude of an absorption feature in emission is a determined by both its optical depth and its spin temperature, which are difficult to disentangle. Furthermore, we are interested in analyzing how well this simple approach recovers the spin temperatures of structures, which we analyze in Section 5.4.1, and therefore we do not impose any requirement that the component amplitudes match at this stage.

In Figure 2, if a structure (left panel) matches with an AGD absorption line (middle panel) and also matches with an AGD emission line (right panel) according to Equations (9) and (10), the circle marker contains a white star and the matching emission line is plotted in the corresponding color (right panel). Of the 6097 structures with AGD absorption line matches, 4228 also have a match to an AGD emission line.

5.3. Quantifying Match Completeness

For most examples in Figure 2, gas structures (left) are accounted for by the majority of the total optical depth along the LOS (middle). This suggests that the AGD absorption lines can be mapped to real structures. However, in the presence of strong line blending, as shown by the third row of Figure 2 (e.g., case i4952), several absorption lines have nearly the same central velocity and the majority of the absorption feature cannot be matched. Although the majority (90%) of LOSs in KOK14 have <2 fitted components, we selected the examples in Figure 2 to illustrate a range in complexity for our fitting and matching process. In particular, the more complex LOSs shown in the bottom three rows of Figure 2, with >2 fitted components, are likely more representative of real observations. We discuss this issue further in Section 6.2.

In Figure 3 we compare the number of structures ($N_{\mathrm{structure}}$) along each LOS with the number of matched AGD-fitted components of the synthetic line profile (N_{AGD}). For each unique value of $N_{\mathrm{structure}}$, the mean (symbol) and standard deviation (shading) of N_{AGD} are shown. Furthermore, we break the sample into latitude bins according to the inset legend. Large symbols indicate the number of AGD absorption matches according Equations (6) and (8), and small symbols indicate the number of AGD absorption *and* emission matches following the subsequent application of Equations (9) and (10).

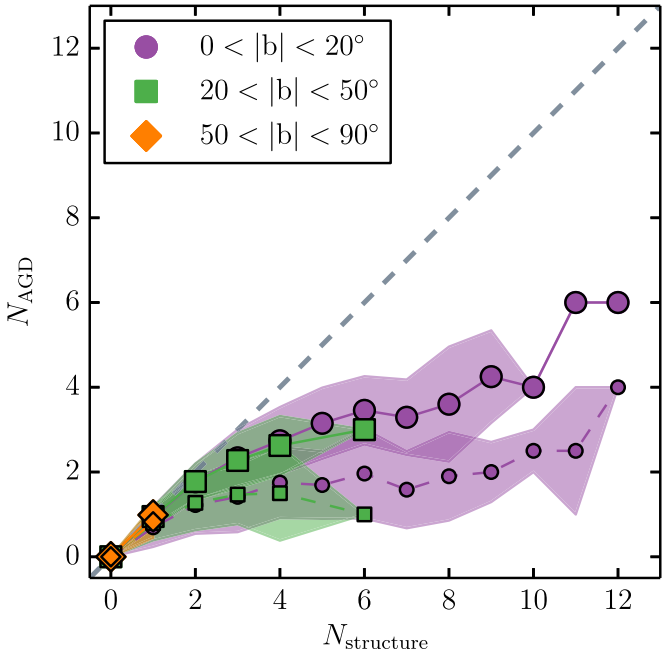

Figure 3. Number of gas structures defined by $n/T_s > 0.002$ cm^{-3} K^{-1} along an LOS ($N_{\mathrm{structure}}$) compared with the number of AGD-fitted features in the synthetic line profile (N_{AGD}). Large symbols show N_{AGD} matched in absorption according to Equations (6) and (8), and small symbols show N_{AGD} matched in absorption and emission according to Equations (6), (8)–(10). Symbols and shading indicate the mean and standard deviations of N_{AGD} for each unique $N_{\mathrm{structure}}$. Samples are binned by latitude according to the inset legend.

Using Figure 3, we quantify the completeness (C) of recovery by

$$C = \frac{\sum N_{\mathrm{AGD}}}{\sum N_{\mathrm{structure}}}. \tag{11}$$

For the matches between gas structures and absorption lines only (large symbols), the completeness for the low ($0 < |b| < 20°$), mid ($20 < |b| < 50°$), and high latitude ($|b| > 50°$) bins are $C_{\mathrm{absorption}} = (0.53, 0.67, 0.99)$ respectively. The recovery is best at the highest latitudes where the number of gas structures and AGD components are smallest and LOS complexity is minimized, allowing for simple and robust AGD fits. At low latitudes, the blending of gas velocities and AGD components makes it difficult to associate unambiguous spectral components with (n/T_s) peaks.

When matching gas structures to H I emission instead of absorption, the recovery completeness is $C_{\mathrm{emission}} = (0.46, 0.53, 0.93)$ for low, mid, and high latitudes, respectively. The completeness is worse in emission than absorption. As observed in Figure 3, broad components associated with high-temperature H I are prominent, thereby making the match to corresponding gas structures more difficult. Although Gaussian analysis has been used extensively in the past to identify gas populations in local and external galaxies, this is among the first statistical quantification of the correspondence between Gaussian H I emission components and individual gas structures.

When matching structures to both absorption and emission (small symbols in Figure 3), the completeness for the low, mid, and high latitude bins is $C_{\mathrm{both}} = (0.29, 0.38, 0.83)$,

respectively. At all latitudes, the structure recovery completeness declines when the match between absorption and emission is performed. The bottom row of Figure 2 displays an example of this decline. Whereas 4/5 structures along the LOS are recovered by AGD absorption components, only 2/4 of those absorption components have matches in emission according to Equations (9) and (10). The structures selected by the matching process with both absorption and emission are biased toward unambiguous features in all three spaces. Nevertheless, the completeness of Gaussian decomposition for the multi-phase structures seen in both emission and absorption is good at $|b| > 50°$. This is certainly promising for future large data sets —even with ∼50% attrition a large number of structures can be retrieved over a wide range of interstellar conditions.

As discussed in the context of Figure 2, in some cases the fraction of total absorption or total emission that can be accounted for by gas structures along the LOS is low. This is especially true when $N_{\rm AGD} \geqslant 2$, although those comprise the minority of cases in KOK14. In the future, improving our selection method for gas structures along the LOS beyond a single cutoff value in (n/T_s) will improve this completeness of structure recovery. In addition, developing additional criteria for structure-component matching based on their amplitudes and/or total column densities will enable us to better quantify the range of gas structures that can be recovered reliably by fitted spectral lines. The analysis presented here represents a first step in our ongoing investigation.

5.4. Observed versus "True" Gas Properties

Given a sample of gas structures with matches to AGD components in absorption and emission, we compare the true temperatures in the simulation with the values inferred from AGD-fitting of the spectra.

5.4.1. Spin Temperature

With the goal of estimating spin temperature automatically for a large number of spectra, we take a more simplified approach than what has been done in HT03 or Murray et al. (2015). For each AGD match between absorption and emission, we start with the isothermal spin temperature as a function of velocity, $T_{s,\rm AGD}(v)$, given by

$$T_{s,\rm AGD}(v) = \frac{T_{B,\rm AGD}(v)}{1 - e^{-\tau_{\rm AGD}(v)}}, \tag{12}$$

where $T_{B,\rm AGD}(v)$ and $\tau_{\rm AGD}(v)$ are the matched set of Gaussian functions fitted by AGD to $T_B(v)$ and $\tau(v)$, respectively. This method assumes a single temperature gas within each velocity channel. To estimate average spin temperature per AGD component, we compute the optical depth-weighted spin temperature per component,

$$T_{s,\rm AGD} \equiv \frac{\int \tau_{\rm AGD}(v) T_{s,\rm AGD}(v) dv}{\int \tau_{\rm AGD}(v) dv}. \tag{13}$$

This approach produces a weighted mean temperature for each component, given that $T_{s,\rm AGD}(v)$ is smaller near the peak of $\tau_{\rm AGD}(v)$ and larger away from it. We note that there are several possible ways to estimate mean temperature from $\tau(v)$ and $T_B(v)$ observations, and some discussion of the pros and cons of each method are given in HT03 and Dickey et al. (2003). It is important to note that Equation (13) works well if, within a multi-phase structure, the CNM and WNM are centered at a similar radial velocity. However, if the CNM is shifted in velocity relative to the WNM due to turbulent motions, so that the peaks of $T_{B,\rm AGD}(v)$ and $\tau_{\rm AGD}(v)$ are slightly offset, Equation (13) will overestimate $T_{s,\rm AGD}$. HT03 and Murray et al. (2015) have allowed for the CNM motion relative to the WNM in their temperature estimates by using a more complex fitting approach where spin temperature is fitted simultaneously with all WNM components. This is, however, computationally expensive for us to implement at this stage.

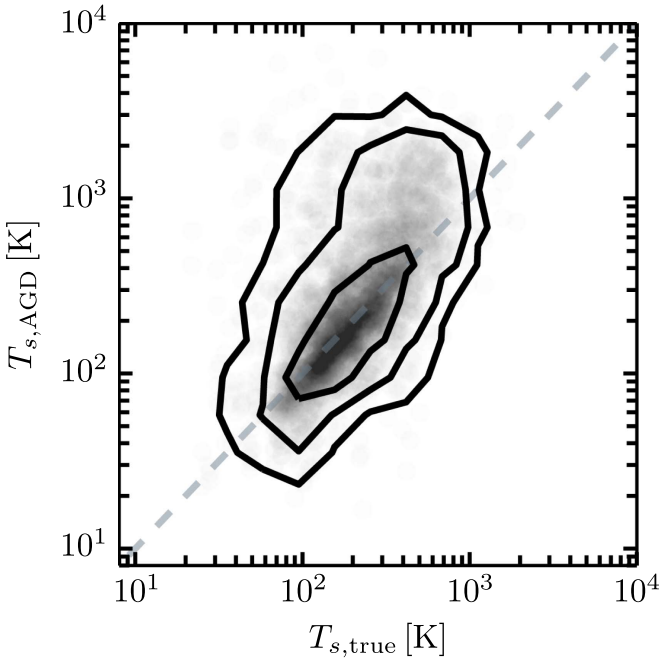

Figure 4. "True" simulated spin temperature ($T_{s,\rm true}$, Equation (14)) vs. inferred spin temperature ($T_{s,\rm AGD}$, Equation (13)) for all structures which match fitted absorption and emission lines according to Equations (6), (8)–(10). Contours indicate the 1, 2 and 3σ limits.

To estimate the temperature of a simulated gas structure, we compute the harmonic mean temperature, $T_{s,\rm true}$, within the pixels spanned by each peak in n/T_s-space. Specifically,

$$T_{s,\rm true} = \frac{\int_{\rm structure} n(s) ds}{\int_{\rm structure} (n/T_s)(s) ds}. \tag{14}$$

In Figure 4, we compare the simulated spin temperature with the inferred spin temperature derived using our radiative transfer approach for all structures with AGD matches in absorption and emission according to Equations (6), (8)–(10). We recover nearly the full range of spin temperatures found in KOK14, which indicates that our structure selection method is likely not missing a significant gas population. Furthermore, the AGD and true estimates agree within the 1σ contours of Figure 4. However, at high temperatures, where $T_{s,\rm true} > 400$ K, the AGD temperature overestimates the true spin temperature.

To understand why AGD overestimates spin temperature at high temperatures, Figure 5 displays a set of example matched spectral lines with $T_{s,\rm true} \sim 400$ K and $T_{s,\rm AGD} \sim 1000$ K. We reproduce the contours from Figure 4 in the top left panel of Figure 5, and include the corresponding matched H I emission and absorption components in the accompanying panels, highlighted with purple shading. In all highlighted cases, the

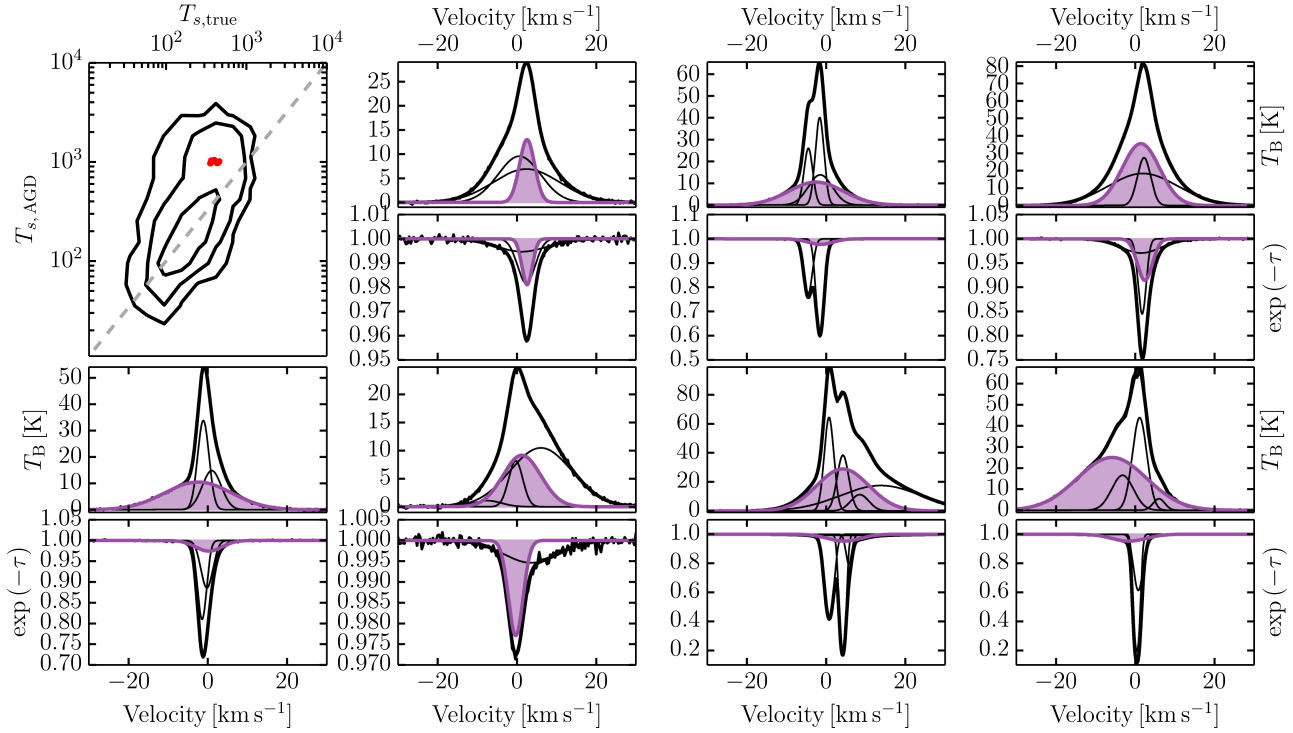

Figure 5. Example synthetic H I emission and absorption spectral pairs in which the AGD-derived spin temperature ($T_{s,\mathrm{AGD}}$) overestimates the simulated spin temperature ($T_{s,\mathrm{true}}$). The top-left panel reproduces Figure 4, with seven examples around $T_{s,\mathrm{true}} = 400$ K and $T_{s,\mathrm{AGD}} = 1000$ K highlighted in red. The matched H I absorption and emission pairs corresponding to these highlighted points are plotted and shaded in purple in the accompanying panels, along with the full AGD decomposition for each spectrum (black).

emission component is slightly offset in velocity from the corresponding absorption component.

As discussed above, this offset is caused by interstellar turbulence. When Equation (13) is applied, the resulting spin temperature will be overestimated if we do not account for this velocity offset. For example, if we estimate the spin temperature using the peak brightness temperature and peak optical depth of highlighted components in Figure 5, we get a value that agrees much more closely with $T_{s,\mathrm{true}}$, since $T_{B,\mathrm{peak}}/(1 - e^{-\tau_\mathrm{peak}}) \sim 400$ K. A more complex radiative transfer treatment such as the method of HT03 and Murray et al. (2015), accounts for this effect, which is strongest for those components with the highest turbulent velocity offset between the CNM and WNM. We find that $T_{s,\mathrm{AGD}}$ most strongly over-estimates $T_{s,\mathrm{true}}$ when the velocity offset between absorption and emission is highest. However, most components are not affected. We will fine-tune our radiative transfer treatment in future work.

5.4.2. Column Density

The H I column density ($N(\mathrm{H\,I})$) is given by

$$N(\mathrm{H\,I}) = C_0 \int T_s(v)\tau(v)dv, \tag{15}$$

where $C_0 = 1.813 \times 10^{18}\,\mathrm{cm^{-2}\,K^{-1}\,(km\,s^{-1})}$. For a pair of matched AGD absorption and emission lines, we compute the column density per component ($N(\mathrm{H\,I})_\mathrm{AGD}$) as

$$N(\mathrm{HI})_\mathrm{AGD} = C_0 T_{s,\mathrm{AGD}} \int \tau_\mathrm{AGD}(v)\,dv, \tag{16}$$

where $T_{s,\mathrm{AGD}}$ is computed using Equation (13) and $\tau_\mathrm{AGD}(v)$ is the Gaussian function fitted by AGD to $\tau(v)$.

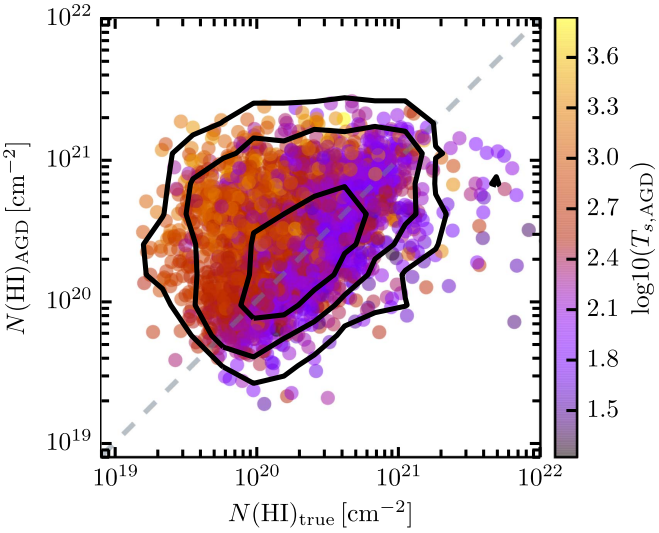

Figure 6. "True," simulated column density ($N(\mathrm{H\,I})_\mathrm{true}$, Equation (17)), vs. "observed" column density ($N(\mathrm{H\,I})_\mathrm{AGD}$, Equation (16)) for all peaks which match fitted absorption and emission components according to Equations (6), (8)–(10). Contours indicate the 1, 2 and 3σ limits.

The simulated column density of each gas structure is given by

$$N(\mathrm{H\,I})_\mathrm{true} = \int_\mathrm{structure} n(s)\,ds. \tag{17}$$

In Figure 6, we compare the "true" and inferred column density for all structures with AGD matches in absorption and emission according to Equations (6), (8)–(10). As in Figure 4, the AGD and true estimates agree within the 1σ contours. However, outside the 1σ contours, $N(\mathrm{H\,I})_\mathrm{AGD}$ overestimates

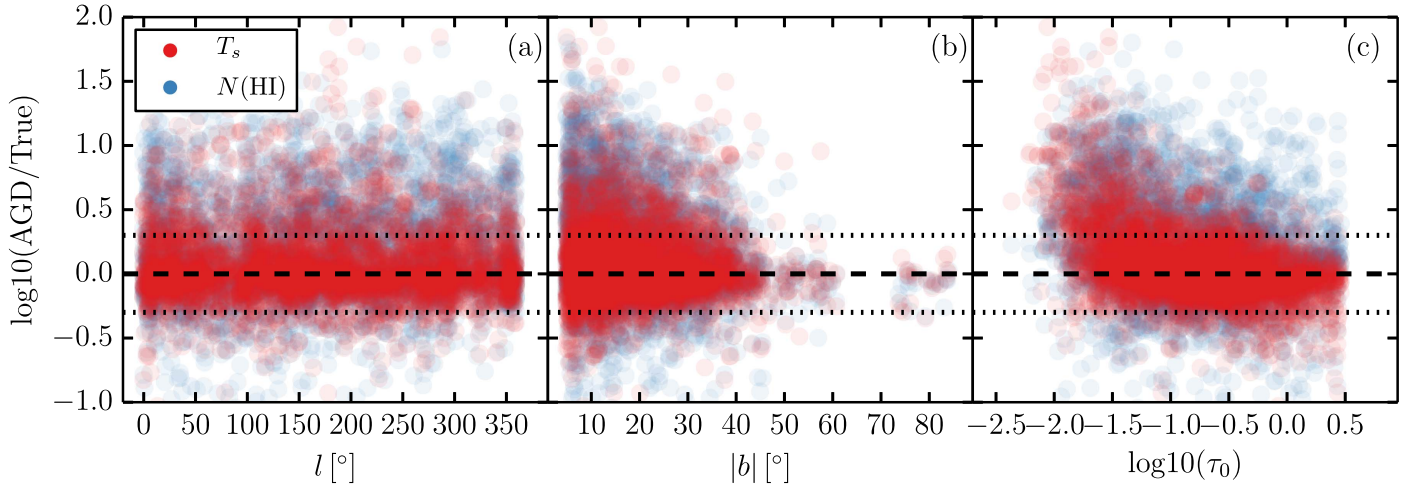

Figure 7. Ratio of inferred ("AGD") to simulated ("true") properties of gas structures matched with Gaussian spectral lines fitted to H I emission and absorption lines as a function of various LOS parameters. (a) Galactic longitude, l [°]; (b) absolute Galactic latitude, $|b|$ [°]; (c) peak optical depth of the matched absorption line, τ_0; spin temperature, $T_{s,\mathrm{AGD}}/T_{s,\mathrm{true}}$ (red) and column density, $N(\mathrm{H\,I})_{\mathrm{AGD}}/N(\mathrm{H\,I})_{\mathrm{true}}$ (blue). Dotted lines indicate factors of 2.

$N(\mathrm{H\,I})_{\mathrm{true}}$, in part because the uncertainty in $T_{s,\mathrm{AGD}}$ is propagated to $N(\mathrm{H\,I})_{\mathrm{AGD}}$ via Equation (16). We color the points in Figure 6 by $T_{s,\mathrm{AGD}}$ to illustrate this. The most discrepant points correspond to the highest values of $T_{s,\mathrm{AGD}}$, where the uncertainty in the matching process is highest (c.f., Figure 4).

In Figure 7, we investigate the scatter present in Figures 4 and 6 by plotting the ratios of the inferred ("AGD") to direct ("true") estimates of spin temperature and column density as a function of various LOS parameters. These include Galactic longitude (l; a), absolute Galactic latitude ($|b|$; b), and the peak optical depth of the matched AGD line (τ_0; c). In each panel, the data points are colored according to $T_{s,\mathrm{AGD}}/T_{s,\mathrm{true}}$ (red) and $N(\mathrm{H\,I})_{\mathrm{AGD}}/N(\mathrm{H\,I})_{\mathrm{true}}$ (blue).

In Figure 7, the ratio of AGD to true spin temperature and column density falls within a factor of 2 for the majority (68%, 1σ contours) of structures at all longitudes (a), latitudes (b), and peak optical depths (c) probed. This indicates that the AGD method is able to recover these properties reasonably well. The scatter in the ratio of AGD to true column density is also larger than for spin temperature, due to the fact that any uncertainty in $T_{s,\mathrm{AGD}}$ is propagated to $N(\mathrm{H\,I})_{\mathrm{AGD}}$ via Equation (16).

The scatter in AGD/true appears to be constant with longitude (l), yet increases at low latitudes ($|b|$) and low peak optical depths ($\tau_0 < 0.1$). This is caused by the increase in LOS complexity at low latitudes, whose effect was noted in Figure 3, and the increased likelihood for a low-τ_0 component to be affected by velocity blending. Examples of strong line blending are shown in Figure 5.

However, the agreement between AGD and true spin temperature and column density for the majority of simulated gas structures given our simple structure selection and matching prescription is encouraging, and indicates that automatic routines for identifying and analyzing spectral components from H I observations—essential for future large observed and simulated data sets—can be successful in recovering true properties for a large fraction of interstellar gas structures.

6. Comparing Real and Synthetic H I Spectra

After analyzing the biases of Gaussian analysis in recovering gas structures and their properties using synthetic spectra from simulations, we proceed to compare observed (21-SPONGE) and simulated (KOK14) H I spectra via AGD-fitted Gaussian parameters.

With the AGD decompositions of H I emission and absorption for all 21-SPONGE and KOK14 LOSs, we apply the criteria described by Equations (9) and (10) to match as many AGD lines between absorption and emission as possible. For KOK14, this does not take into account matching with gas structures along the LOS as described in Section 5, in the interest of eliminating as many biases as possible in our comparison between the matching statistics of KOK14 and 21-SPONGE (which does not have LOS density and temperature information for defining structures).

Figure 8 displays the matches between H I absorption and H I emission for a set of five example observed LOSs from 21-SPONGE. All components fitted by AGD to each LOS are shown in dashed black, and the components which satisfy the matching criteria described by Equations (9) and (10) are shown in colors.

6.1. Number of Components along LOSs

In Table 1 we list the total number of AGD components in each H I absorption and emission data set, as well as the mean and standard deviation of the number of components (N_{AGD}) per LOS. In addition, we list the total number of matched components between absorption and emission, and the mean and standard deviation number of matches per LOS.

From Table 1, the mean value of N_{AGD} is more than a factor of two greater for the observed 21-SPONGE H I absorption and emission spectra than KOK14, despite large scatter. Figure 9 displays histograms of N_{AGD} for 21-SPONGE (top left panel) and KOK14 (bottom left panel) absorption (black solid) and emission (orange dashed) components. In agreement with the statistics shown in Table 1, the maximum number of components fitted to 21-SPONGE absorption (12) is a factor of two higher than KOK14 (6).

In the right panels of Figure 9, we account for the effect or different viewing angles by multiplying N_{AGD} by $\sin|b|$ for all 21-SPONGE and KOK14 components. This quantity is the effective number of components in the vertical direction of the simulated or observed volume. Since $N_{\mathrm{AGD}} \times \sin|b|$ is still

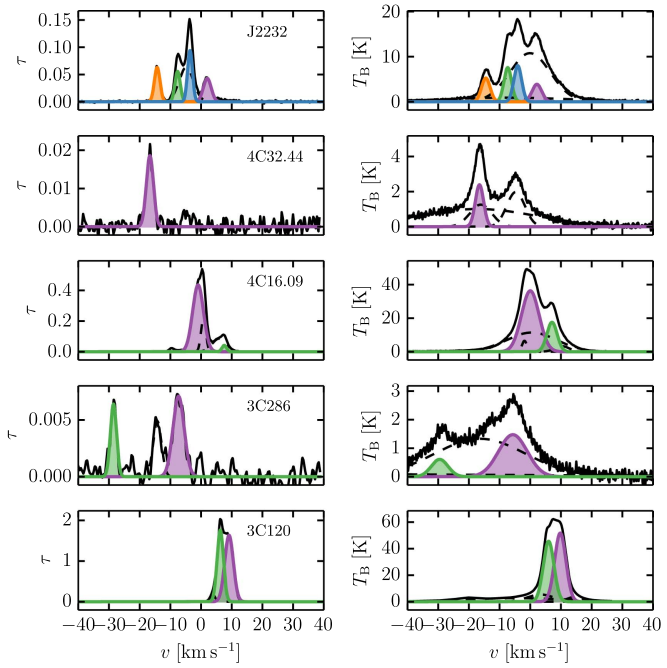

Figure 8. Example LOS H I absorption spectra (left) and corresponding H I emission spectra (right) from 21-SPONGE, with AGD-fitted Gaussian decompositions overlaid (dashed black). Components which match between absorption (left) and emission (right) according to Equations (9) and (10) are indicated by matching colors between the left and right columns.

larger for the 21-SPONGE than KOK14, it suggests that the discrepancy between is not a $\sin|b|$ effect.

The larger number of components found in the 21-SPONGE spectra, after correcting for observing angle, indicates that the velocity range used to produce the KOK14 synthetic spectra is smaller than what is sampled by observations. The KOK13 simulations are known to have a relatively low vertical velocity dispersion (∼5–7 km s^{-1}), somewhat smaller than observed values. The lower velocity dispersion also yields a scale height somewhat smaller than observations. We will return to this effect in Section 6.2.2. In more recent simulations (Kim & Ostriker 2016) with a better treatment for supernovae, velocity dispersions are in fact larger, and it will be interesting to test whether this will lead to an increase in the number of AGD features per LOS.

We emphasize that the results shown in Figure 9 are derived from identical implementation of AGD to real and synthetic H I spectra, and thus the comparison is unaffected by biases introduced in spectral line analysis. Therefore, although the caveats described above are known from external analysis of the KOK13 simulations, Figure 9 suggests that $N_{\rm AGD}$ reflects the total velocity range and path length.

Furthermore, from Table 1, although the number of matches per LOS is consistent with the number of fitted lines per LOS ($N_{\rm AGD}$) in KOK14, there are comparatively fewer matches per LOS than $N_{\rm AGD}$ in 21-SPONGE. This difference likely comes from the so-called mismatch of angular resolution. In 21-SPONGE, the angular resolution of the H I absorption measurements is determined by the size of the background source, not the telescope beam (and is therefore <1–40″). However, the H I emission spectrum has an angular resolution of 3.′5. Therefore, the H I emission spectrum may not sample the same structures seen in absorption, especially if there is significant emission structure on angular scales below the resolution limit. This mismatch complicates the matching process and causes a larger attrition rate for observations. Simulations, on the other hand, do not suffer from this problem, as emission and absorption are derived using the same angular resolution. In the future, we plan to quantify this effect by smoothing simulated spectra, and we further compare the 21-SPONGE and KOK14 emission properties in detail in Section 6.3.

6.2. Properties of H I Absorption Components

To compare 21-SPONGE and KOK14, Figure 10 displays cumulative distribution functions (CDFs) of Gaussian parameters fitted by AGD to H I absorption spectra observed by 21-SPONGE (black) and simulated by KOK14 with (blue) and without (orange) the WF effect, normalized by the total number of components (see Table 1). These parameters include amplitude (τ_0; left panel), FWHM (Δv_0 in km s^{-1}; center panel), and mean velocity (v_0 in km s^{-1}; right panel). For each data set, we also plot the CDFs of 1000 bootstrapped samples (shown in lighter-shaded colors according to the legend) to illustrate the effect of sample size and outliers on the shape of the CDF.

6.2.1. Comparison with Previous Studies

We include the results of the by-hand Gaussian decomposition of the first 31/52 21-SPONGE sources (dashed purple; Murray et al. 2015, "DR1") and the Millennium Arecibo 21 cm Absorption Line Survey (dashed green; HT03) in Figure 10. With lower sensitivity in optical depth, the HT03 distribution contains fewer $\tau_0 < 10^{-2}$ components than are found in the 21-SPONGE or KOK14 AGD decompositions. However, the 21-SPONGE DR1 τ_0 distribution agrees very well with the 21-SPONGE AGD distribution, which indicates that although the AGD algorithm was trained using component parameters from HT03, it is successfully able to recover lower-τ amplitudes found in the higher-sensitivity 21-SPONGE and KOK14 spectra. This agreement was also noted in the comparison between by-hand and AGD analysis of a subset of the 21-SPONGE sample (Lindner et al. 2015). In addition, the 21-SPONGE AGD Δv_0 distribution agrees very well with DR1 and HT03, indicating that for a wide range in optical depth sensitivity, a similar range in Gaussian spectral line widths can be recovered.

6.2.2. Influence of Local Box Simulations

From the right-hand panel of Figure 10, the observed 21-SPONGE (AGD and DR1) and HT03 absolute mean velocities ($|v_0|$) agree very well. However, the KOK14 spectra are dominated by components with $v_0 < 10$ km s^{-1}. This difference may be caused by the fact that the KOK14 spectra are constructed with a limited path length ($s < 3$ kpc) based on their local box simulations, in which the sources of H I lines are limited by nearby gas with small variations of galactic rotation velocity. The limited range of v_0 in KOK14 spectra causes more components to have similar central velocity.

To test the influence of the local box and lack of global rotation effects in the simulation, we consider the effect of latitude on the matching statistics. For high latitude LOSs ($|b| > 50°$) in KOK14, the number of absorption fits, emission fits, and matches per LOS are consistent with the full KOK14 sample (i.e., all latitudes). However, for 21-SPONGE, at high latitudes ($|b| > 50°$) there are 1.9 ± 1.1 absorption fits per

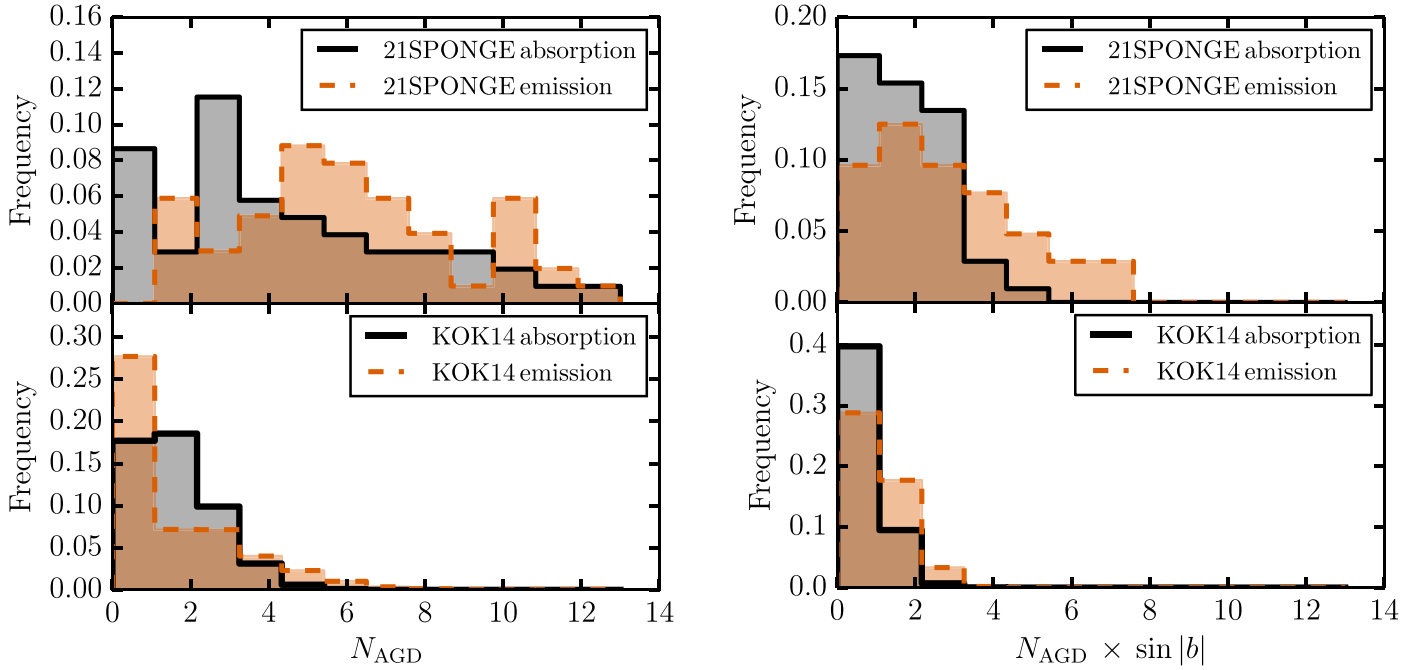

Figure 9. Left: histograms displaying number of AGD lines ($N_{\rm AGD}$) fit to H I absorption (black) and emission (orange) observations from 21-SPONGE (top) and synthetic observations by KOK14 (bottom). Right: histograms displaying number of AGD lines per unit path length in the "vertical" direction ($N_{\rm AGD} \times \sin|b|$) for H I absorption (black) and emission (orange) observations from 21-SPONGE (top) and synthetic observations by KOK14 (bottom).

LOS, 4.4 ± 1.7 emission fits per LOS, and 0.9 ± 0.9 matches per LOS, which are more consistent with the full KOK14 sample than with the full 21-SPONGE sample (c.f., Table 1). With increasing latitude, the effect of galactic rotation on spectral line properties declines. The consistency in matching statistics between 21-SPONGE and KOK14 at high latitudes suggests that simulated Galactic rotation dynamics play an important role in the differences between observed and simulated spectral line properties at low latitudes. Therefore, the Gaussian fitting process and match between emission and absorption (Equations (9) and (10)) in KOK14 likely suffer from more completeness issues than in observed 21-SPONGE spectra at low latitudes. This also suggests that our completeness statistics in Section 5.3 will be improved in future simulations, in which a larger box and more realistic supernova feedback are implemented to push gas to higher scale heights and a wider range in velocity.

6.2.3. Minimum CNM Temperature?

To highlight the comparison between 21-SPONGE and KOK14 we plot τ_0 versus Δv_0 in Figure 11, including marginal histograms of both parameters. The median 1σ sensitivity limit in τ is indicated by the dashed horizontal line ($\sigma_\tau = 10^{-3}$), and the 21-SPONGE velocity resolution of 0.4 km s^{-1} is indicated by the dashed vertical line.

From the top panel of Figure 11, we observe a sharp cutoff in $\Delta v_0 \sim$ 1–2 km s^{-1} in 21-SPONGE and KOK14.[5] If we assume a limiting line width of ∼1–2 km s^{-1}, in the case of no turbulent broadening, the corresponding CNM kinetic temperature is ∼20–30 K, which is also equal to the spin temperature. The fact that 21-SPONGE and KOK14 agree in their lower limit to Δv_0, together with the fact that the AGD method is a good measure of $T_{s,\rm true}$ at similar temperatures (c.f., Figure 4), suggest that the simulation and observations have a similar lower limit for the CNM temperature of ∼20–30 K.

As shown in Figure 11, the peak optical depth spans the whole parameter space all the way to our sensitivity limit with no obvious evidence for the existence of a minimum optical depth for the CNM. In addition, only a small fraction, <10%, of components have $\tau_0 > 1$ in KOK14 and 21-SPONGE.

6.2.4. Role of the WF Effect

As seen most clearly in the main panel of Figure 11, the KOK14 spectra with and without the WF effect include significant populations of components with $\Delta v_0 > 10$ km s^{-1} and $0.001 < \tau_0 < 0.01$. Although this region is located well above the 21-SPONGE median sensitivity in optical depth, we find very few 21-SPONGE components there. In addition, in KOK14, these components are often found without narrow (CNM-like) components superimposed along the same LOS. This is a type of profile not seen in 21-SPONGE observations. There are no observational biases that would prevent us from seeing simple Gaussian line profiles with a peak optical depth of ∼0.01 and a velocity FWHM of ∼10 km s^{-1}. In addition, the lack of isolated (devoid of CNM), broad, WNM-like features in observations is supported by additional high-sensitivity H I absorption studies (e.g., HT03, Roy et al. 2013). An example isolated, broad absorption line from KOK14 is shown in the top row of Figure 2.

We note that these broad, low-τ features appear in the synthetic KOK14 spectra regardless of our treatment of the WF effect, although agreement with observations is somewhat improved when the WF effect is included (c.f., Figure 11). The origin of these low-τ_0 components is not well understood and future comparisons with synthetic 21 cm profiles from simulations will explore the effect of a more realistic feedback treatment (e.g., Kim & Ostriker 2016). The present results

[5] We note that the components with $\Delta v_0 < 1$ km s^{-1} in 21-SPONGE and KOK14 are likely spurious fits, given that the accuracy of the AGD decomposition is known to be 80% in absorption (c.f., Section 4).

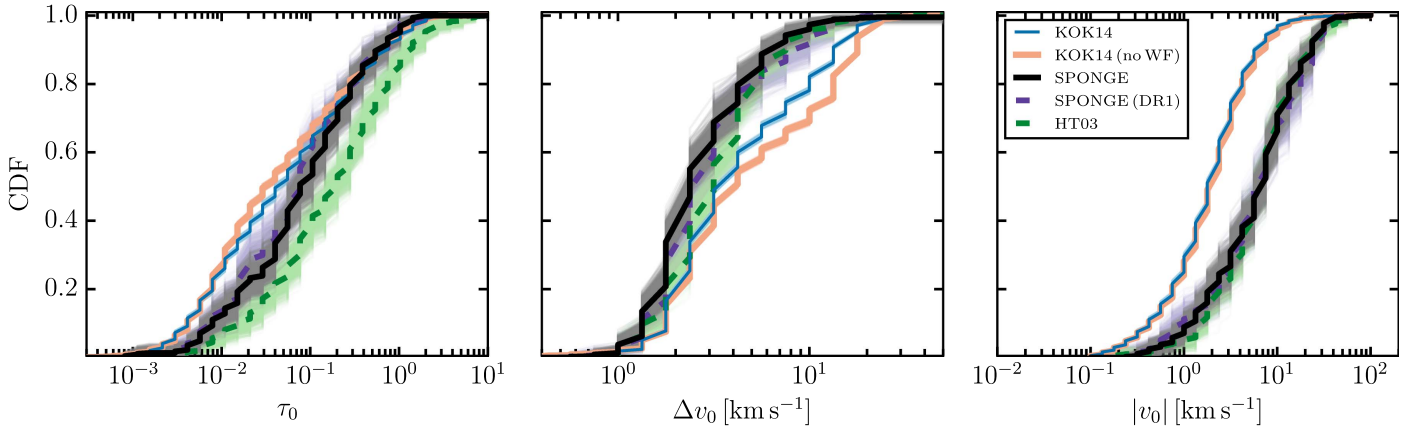

Figure 10. Cumulative distribution functions (CDFs) of Gaussian parameters, including optical depth amplitude (τ_0), FWHM (Δv_0), and absolute mean velocity ($|v_0|$), of the components fitted by AGD to observed (21-SPONGE) and synthetic (KOK14) H I absorption spectra, including previous by-hand results from 21-SPONGE (purple dashed line, DR1; (Murray et al. 2015) and HT03 (green dashed line) for comparison. For each data set, we plot the CDFs of 1000 bootstrapped samples (shown in lighter-shaded colors according to the legend) to illustrate the effect of sample size and outliers on the CDF.

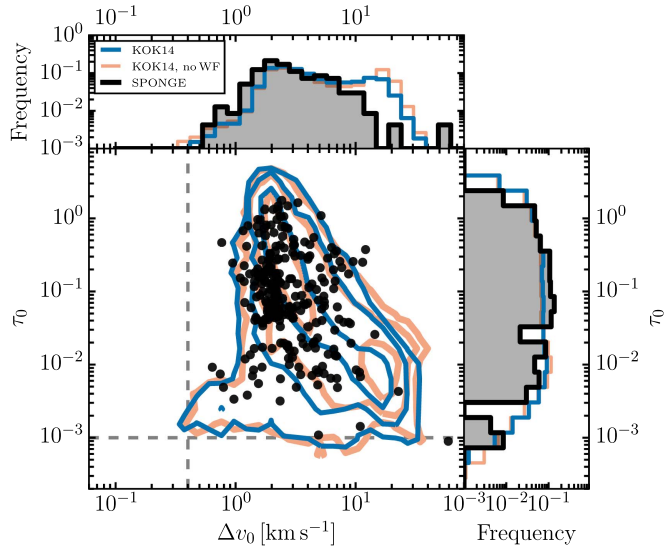

Figure 11. Parameters of Gaussian components (Δv_0, τ_0) fitted by AGD to H I absorption spectra from 21-SPONGE (black) and KOK14 with the WF effect (blue) and without the WF effect (orange). Contours indicate the 1, 2, and 3σ limits for the KOK14 distributions. Marginal histograms display the same results according to the legend.

already suggest that H I absorption spectra may be able to provide discriminating tests of the input physics in simulations.

6.3. Properties of H I Emission Components

Before comparing the properties of H I emission components in the same manner as in our comparison of absorption components in Section 6.2, we emphasize again that the 21-SPONGE and KOK14 emission profiles are derived from different angular scales. The angular resolution of the KOK14 emission spectra is the same as for the absorption lines. However, the 21-SPONGE emission spectra were observed with the Arecibo radio telescope, with a $\sim$3.′5 beam at 21 cm derived from off-target positions, and therefore have different angular resolution than the 21-SPONGE VLA absorption spectra. In the case of the KOK14 spectra, which are derived from a simulation with a physical resolution of 2 pc, the path length would need to be longer than $\sim$2 kpc to achieve better angular resolution than 21-SPONGE. Therefore, for shorter LOSs at predominately higher latitudes, the angular resolution of synthetic emission spectra is actually worse than 21-SPONGE observations. We stress that absorption lines do not have the resolution problem and this is also the reason why they are more suitable for comparison with simulations.

Figure 12 displays CDFs of Gaussian parameters from the fits to H I emission spectra observed by 21-SPONGE (black) and simulated by KOK14 with the WF effect (blue) and without the WF effect (orange), in addition to the results of HT03 (green) and 21-SPONGE DR1 (purple). These parameters include amplitude in brightness temperature ($T_{B,0}$ in K; left), FWHM ($\Delta v_{0,\rm em}$ in km s^{-1}; center), and mean velocity ($v_{0,\rm em}$ in km s^{-1}; right). To illustrate the comparison between 21-SPONGE and KOK14 further, we display $T_{B,0}$ versus $\Delta v_{0,\rm em}$ for 21-SPONGE and KOK14 in Figure 13, with marginal histograms for both parameters. We note that the WF effect does not make a difference to components fitted to H I emission spectra (i.e., orange and blue lines are indistinguishable in Figure 12). This indicates that future testing of the implementation of the WF effect should use absorption, rather than emission spectra.

6.3.1. Boundaries in Brightness Temperature

In the left panel of Figure 12 (as well as Figure 13), the amplitudes fitted by AGD to 21-SPONGE agree well with 21-SPONGE DR1 and HT03. All three data sets were obtained using the Arecibo radio telescope, and therefore they have similar angular resolution. However, all three observed distributions are shifted to slightly lower amplitude in brightness temperature ($T_{B,0} < 10$ K) relative to KOK14 in Figure 12. For the KOK14 LOS with lower effective angular resolution than 21-SPONGE, the synthetic brightness temperature spectrum averages any simulated emission over larger solid angles, and therefore the KOK14 $T_{B,0}$ should tend to be smaller than the 21-SPONGE values derived from smaller angular scales. However, we observe more low-$T_{B,0}$ components in 21-SPONGE than KOK14.

The slight excess of components with high $T_{B,0}$ and low Δv_0 in KOK14 may be caused by the lack of chemistry and H I-to-H_2 transition in the simulation. Furthermore, as noted previously, the relative lack of high-Δv_0 components in KOK14 may be partly attributed to the reduced velocity

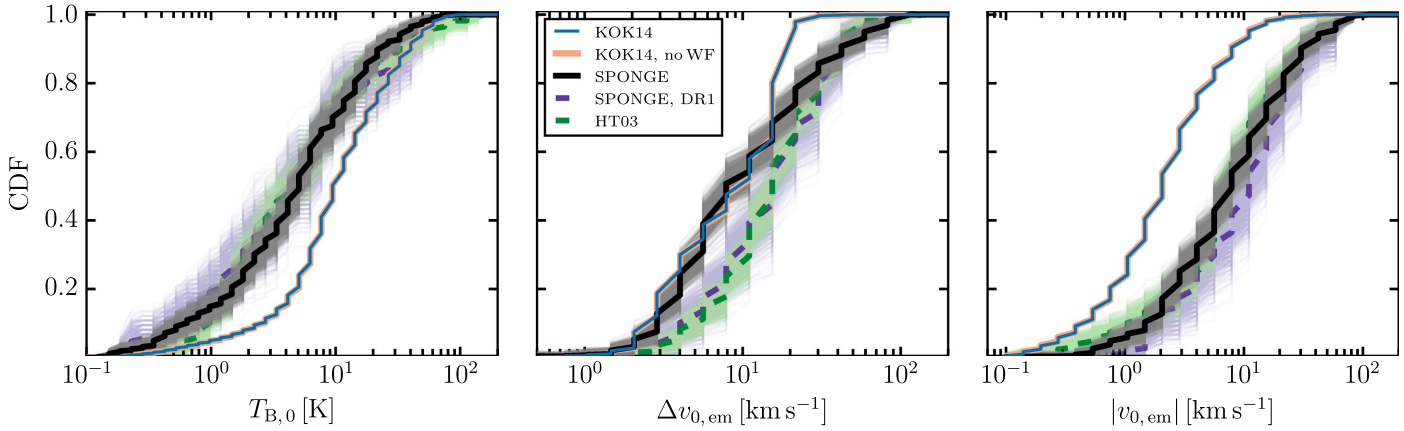

Figure 12. CDFs of Gaussian parameters, including brightness temperature amplitude (T_B), FWHM (Δv_0), and mean velocity (v_0), of the components fitted to observed (21-SPONGE) and synthetic (KOK14) H I emission spectra, including previous by-hand results from 21-SPONGE (purple dashed line, DR1; Murray et al. 2015) and HT03 (green dashed line) for comparison. For each data set, we plot the CDFs of 1000 bootstrapped samples drawn from the full sample with replacement (shown in lighter-shaded colors according to the legend) to illustrate the effect of sample size and outliers on the CDF.

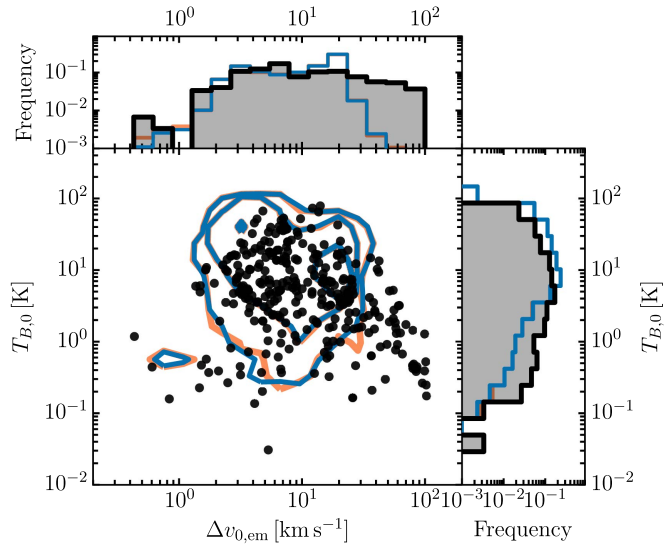

Figure 13. Parameters of Gaussian components (FWHM, $T_{B,0}$) fitted by AGD to H I emission spectra from 21-SPONGE (black) and KOK14 with the WF effect (blue) and without the WF effect (orange). Contours indicate the 1, 2, and 3σ limits for the KOK14 distributions. Marginal histograms display the same results according to the legend.

dispersion in the simulations compared to observations. Our observations may even suggest an upper-limit on $T_{B,0}$ of ~60–70 K. In addition, on the low-end of the distribution the absence of a large filling-factor (~50%) hot ($T \sim 10^5$–10^7 K) medium in the simulations produces too much neutral gas per LOS, and therefore too few LOSs with $T_{B,0} <$ a few K. The presence of a hot medium occupying a large fraction of the volume would also tend to reduce the incidence of detectable low-τ_0 features, since many of the LOSs without CNM would be primarily hot rather than primarily warm medium.

6.3.2. Broad Emission Components

In the middle panel of Figure 12, the 21-SPONGE and KOK14 $\Delta v_{0,\rm em}$ distributions agree very well below $\Delta v_{0,\rm em} \sim 10$ km s^{-1}. However, the 21-SPONGE AGD, DR1, and HT03 distributions extend to higher values of $\Delta v_{0,\rm em}$ than KOK14. This is especially noticeable in Figure 13 where 21-SPONGE components with large $\Delta v_{0,\rm em}$ and small $T_{B,0}$ form a prominent tail of the distribution. As discussed previously, the 21-SPONGE H I emission observations have not been corrected for stray radiation, which would appear in the form of weak and broad spectral components. To test how many 21-SPONGE components could be affected by stray radiation, we extracted H I emission spectra from the stray-radiation-corrected LAB survey (Kalberla et al. 2005) at the positions of our sources and implemented AGD in the same manner to decompose the LAB spectra into Gaussian components. Consequently, LAB data contain many components with $\Delta v_{0,\rm em} \sim$ 10–70 km s^{-1} (c.f., the Appendix). However, components with $\Delta v_{0,\rm em} \gtrsim 70$ km s^{-1} are not seen in LAB data, and therefore those components in 21-SPONGE are likely caused by stray radiation. There are nine such components and they are all located in the large $\Delta v_{0,\rm em}$ and small $T_{B,0}$ tail. Peek et al. (2011) did a similar comparison between LAB and Arecibo data and concluded that the effect is unlikely to exceed 500 mK, in agreement with our with our conclusion that the broadest 21-SPONGE components with $T_{B,0} < 0.5$ K are likely caused by stray radiation.

This leaves a population of broad ($\Delta v_{0,\rm em} \gtrsim$ 20–70 km s^{-1}), shallow ($T_{B,0} < 10$ K) components that are prominent in 21-SPONGE but absent in KOK14. Possibly a higher velocity dispersion and the inclusion of a Galactic fountain in the simulation (see e.g., Kim & Ostriker 2016) may be able to reproduce such broad lines. Alternatively, this could signify the presence of the WNM at temperature >4000 K. For example, Murray et al. (2014) detected a residual absorption component with a width of 50 km s^{-1} and $T_s \sim 7000$ K by stacking the first third of the 21-SPONGE data. Further work is clearly needed to understand the origin of such broad emission components, as well as to remove stray radiation from Arecibo spectra.

Finally, in the right panel of Figure 12, all observed H I emission spectra have absolute mean velocities up to ~50 km s^{-1}, whereas the KOK14 mean velocities appear limited to $v_{0,\rm em} < 10$ km s^{-1} (c.f., right panel Figure 10). In addition to the nature of the local box reducing $|v_{0,\rm em}|$, the KOK13 simulations did not include a Galactic fountain of WNM with velocities up to tens of km s^{-1}. The inclusion of

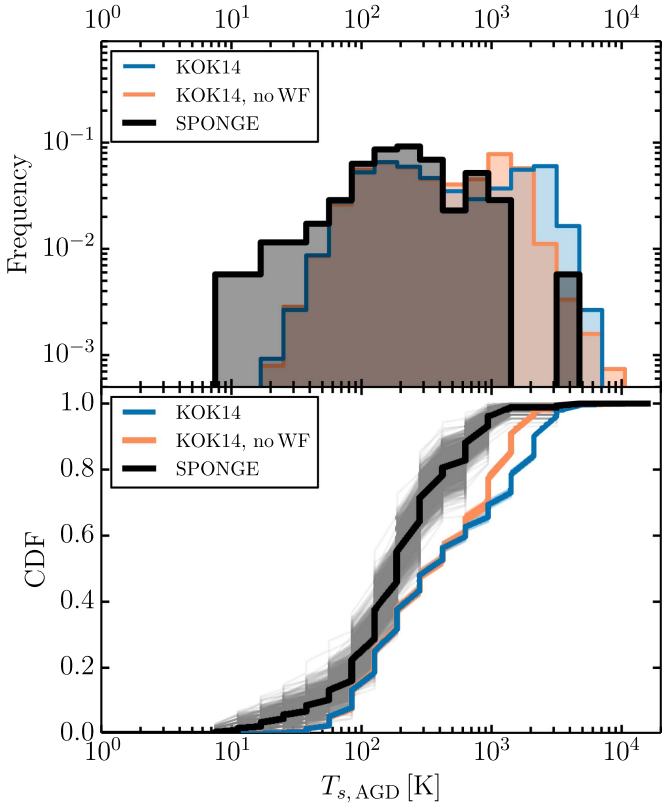

Figure 14. Top: histograms of $T_{s,\mathrm{AGD}}$ (Equation (13)) for all components which "match" between H I emission and absorption (Equations (9) and (10)) following the AGD analysis of 52 21-SPONGE H I spectral pairs (thick, solid black) and 9355 KOK14 H I spectral pairs with the WF effect (thin, solid blue) and without the WF effect (thin, solid orange). Bottom: CDFs of the same results, with 1000 bootstrapped samples drawn from the full sample with replacement (shown in lighter-shaded colors according to the legend) to illustrate the effect of sample size and outliers on the CDF.

this important mechanism may produce relatively more structures with larger $|v_{0,\mathrm{em}}|$ and $\Delta v_{0,\mathrm{em}}$ and improve similarities between the 21-SPONGE and simulation results.

6.4. Observed Spin Temperature

We now compare distribution functions of the inferred spin temperature, from 21-SPONGE spectra and KOK14 synthetic spectra. As we have shown in Section 5.4.1, for the majority of cases the inferred spin temperature using our AGD and radiative transfer approach, $T_{s,\mathrm{AGD}}$, is in agreement with the true simulated temperature, $T_{s,\mathrm{true}}$. We also discussed how at >400 K, $T_{s,\mathrm{AGD}}$ over-estimates $T_{s,\mathrm{true}}$. However, this bias will affect both observations and simulations in the same way, as we apply the same AGD fit and radiative transfer method to KOK14 and 21-SPONGE. In addition, our main focus in this paper is on the shape of distribution functions, not the exact fractions. In future work, we will focus on the fractions of H I in CNM, WNM, and unstable phases using updated simulations.

Figure 14 displays histograms and CDFs of $T_{s,\mathrm{AGD}}$ (Equation (13)) for 21-SPONGE (black) and KOK14 with (blue) and without (orange) the WF effect. The observed and simulated $T_{s,\mathrm{AGD}}$ distributions follow each other well until $T_{s,\mathrm{AGD}} \sim$ 400–500 K, when they start to diverge. Although the 21-SPONGE observations appear to have a higher relative fraction of components at low $T_{s,\mathrm{AGD}} \sim$ 20–30 K, these bins

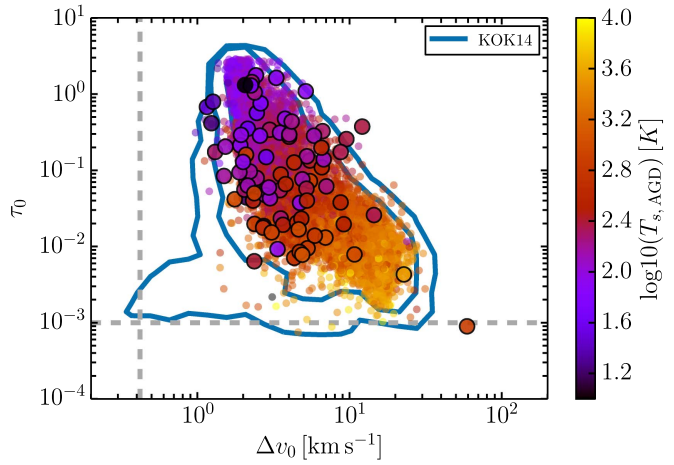

Figure 15. AGD absorption properties (τ_0, Δv_0) for all components fitted to KOK14 with the WF effect (blue contours), and all components which match between absorption and emission according to Equations (9) and (10) for KOK14 (small circles) and 21-SPONGE (large circles with black outlines), colored by the AGD spin temperature ($T_{s,\mathrm{AGD}}$).

are determined by small number of components, and the fractions agree within uncertainties as illustrated by the bootstrapped samples shown in the CDF panel. As discussed in Section 6.2, the observations and simulations display consistent cutoff in CNM line width, and Figure 14 indicates that the fractions of material at corresponding spin temperatures of 20–30 K are consistent. HT03 detected a similar population of cold CNM components with $\lesssim$20 K (17% by number, and 4% by mass), and suggested that this is evidence for the absence of photoelectric heating by dust (Wolfire et al. 1995). We note that the simulations have uniform heating throughout and constant metallicity, while in reality the photoelectric heating would be reduced in high-column regions.

However, the KOK14 spectra show more H I with $T_{s,\mathrm{AGD}} =$ 300–3000 K than 21-SPONGE. To illustrate the types of components with these temperatures, in Figure 15 we reproduce Figure 11, including the total contours with WF from KOK14 and all matched components from KOK14 (small circles) and 21-SPONGE (large circles with black outlines), colored by $T_{s,\mathrm{AGD}}$. The AGD components with $T_{s,\mathrm{AGD}} \sim$ 300–3000 K in KOK14 have lowest optical depth and the largest FWHM. These are exactly the components discussed in Section 6.2 to have simple, broad profiles without overlapping CNM components—a type of spectral profile which is not found often in 21-SPONGE.

Are the differences shown in Figures 14 and 15 caused by observational sensitivity? 21-SPONGE was designed with the goal of detecting warm H I in absorption and has excellent optical depth sensitivity (rms noise $\sigma_\tau < 10^{-3}$ per channel; Murray et al. 2015). To estimate the temperatures we are sensitive to in 21-SPONGE observations, we assume a WNM column density of a few $\times 10^{20}$ (e.g., Stanimirović et al. 2014, KOK14), an FWHM of 10–20 km s^{-1}, and a conservative rms sensitivity in optical depth of $10^{-2} - 3 \times 10^{-3}$ (per 0.4 km s^{-1} velocity channels), which results in $T_s \sim$ 1000–6000 K. This is the range of what is expected by KOK14 and also Liszt (2001). Therefore, 21-SPONGE has the observational sensitivity to detect spectral components with $T_s >$ 1000 K. In Section 5.4.1, we demonstrated that our AGD and radiative transfer implementation are not biased against WNM, and in fact above ~400 K tend to overestimate the true spin temperature. Therefore, we infer that the lack of observed

components with $T_s > 1000$ K is not affected by sensitivity or analysis method. In addition, we emphasize again that the $T_s > 1000$ K components in simulations have isolated, simple spectral profiles that we do not find in observations.

To further test the effect of observational sensitivity on the inferred spin temperature, Murray et al. (2014) investigated methods for improving the 21-SPONGE sensitivity to broad, shallow WNM-like absorption with high temperature. We stacked residual H I absorption lines of a subset of sources following by-hand Gaussian decomposition and found a residual H I absorption signal at 5σ significance with an inferred excitation temperature of $T_s = 7200^{+1800}_{-1200}$ K, with an FWHM of 50 km s^{-1}, and an H I column density of 2×10^{20} cm^{-2} (Murray et al. 2014). This temperature is higher than analytical predictions for collisional excitation of H I, and indicates that additional H I excitation mechanisms (e.g., the WF effect) may be more important for coupling the hyperfine spin states of H I to the local thermodynamic temperature than previously thought.

If the spin temperature of the WNM is actually $T_s \sim 7000$ K (Murray et al. 2014), rather than $2000 < T_s < 4000$ K as inferred currently from analytical models of collisional excitation (e.g., Liszt 2001), then it is possible that individual 21-SPONGE spectra may still lack sensitivity for detecting the WNM. Even more sensitive observations, as well as further stacking analysis, will be essential from an observational standpoint. This result shows that understanding the implementation of the WF effect in numerical simulations, and in particular the highly uncertain n_α, its spatial variations across the Milky Way, as well as the effect of turbulence, is essential to reconcile H I observations and theory.

6.4.1. Per-channel T_s

Instead of using Gaussian-based temperature estimates, KOK14 considered per-channel spin temperature in their analysis of simulated H I properties. They found that this quantity agrees with the true per-channel temperature extremely well (within a factor of 1.5) for all channels with $\tau \lesssim 1$ (KOK14). Several observational studies have also used per-channel temperature estimates to analyze H I phases (e.g., Roy et al. 2013). To compare with their results, we derive per-channel spin temperature, $T_{s,\mathrm{obs}}(v)$, by applying an equation similar to Equation (12) to the full $\tau(v)$ and $T_B(v)$ spectra from 21-SPONGE and KOK14, where

$$T_{s,\mathrm{obs}}(v) = \frac{T_B(v)}{1 - e^{-\tau(v)}}. \quad (18)$$

For each LOS, we compute $T_{s,\mathrm{obs}}(v)$ for only those channels with optical depths greater than 3×10^{-3}, to conservatively exclude all channels with low S/N.

In Figure 16, we display histograms and CDFs of $T_{s,\mathrm{obs}}(v)$ for 21-SPONGE (black) and KOK14 with (blue) and without (orange) the WF effect. There is a similar discrepancy between observations and simulations in Figure 16 as seen in Figure 14. The KOK14 distributions are shifted to higher temperatures, while 21-SPONGE spectra contain more channels with low temperature (<200 K). In addition, the 21-SPONGE CDF has a more gradual rise, while simulated data show an abrupt jump near $T_{s,\mathrm{obs}}(v) \sim 1000$ K suggesting that most simulated LOSs are dominated by higher $T_{s,\mathrm{obs}}(v)$ derived from spectral channels without detectable absorption. It is important to keep in mind, however, that observed and simulated spectra probe different LOS lengths, as discussed in Section 6.2, which could affect the shape of per-channel CDFs. In addition, the absence of a hot medium in the present simulations may lead to too many LOSs with $T_s \sim 1000$ K.

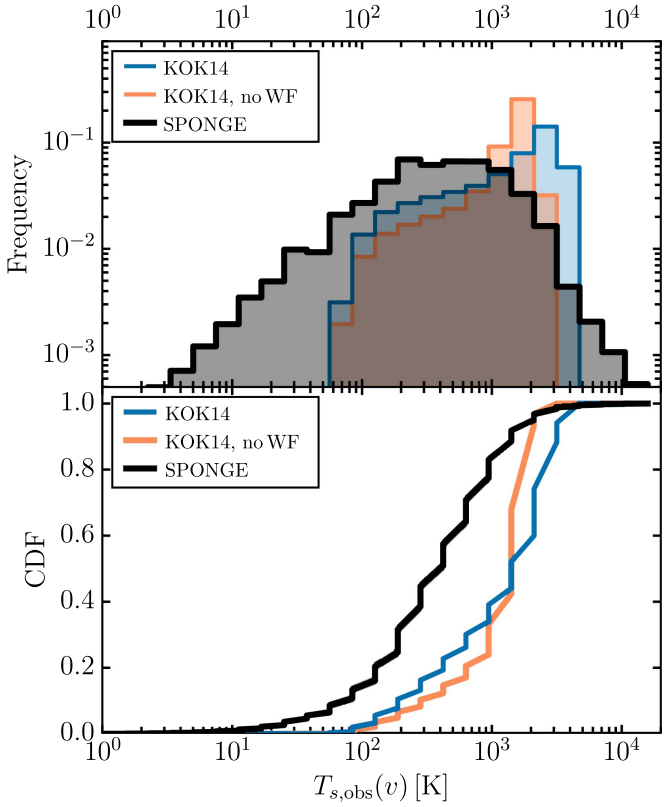

Figure 16. Top: histograms of per-channel spin temperature ($T_s(v)$) for all 52 21-SPONGE H I spectral pairs (thick, solid black) and 9355 KOK14 H I spectral pairs with the WF effect (thin, solid blue) and without the WF effect (thin, solid orange). Bottom: CDFs of the same results.

6.5. Observed Column Density

As a further benefit of AGD analysis, by resolving the properties of individual spectral components along each LOS, we can analyze the column densities of individual gas structures in contrast with the total LOS column density. In Figure 17, we display histograms and CDFs of $N(\mathrm{H\,I})_{\mathrm{AGD}}$ for individual matched spectral components from the KOK14 (blue) and 21-SPONGE (thick black) H I emission and absorption spectral pairs. The column density distributions shown in Figure 17 agree well at high-$N(\mathrm{H\,I})$ ($>10^{20}$ cm^{-2}), although the 21-SPONGE distribution extends further below $N(\mathrm{H\,I}) = 10^{19}$ cm^{-2}.

The absence of low-column lines in the KOK14 spectra may be caused by insufficient angular resolution for detecting small CNM features, or, as has been mentioned throughout, the absence of a hot medium in the KOK13 simulations which would serve to reduce the observed column densities of the matched lines. The discrepancy around 10^{20} cm^{-2} is likely caused by the discrepancy in $T_{s,\mathrm{AGD}}$ discussed above in Section 6.4. It is interesting to note that the application of the WF effect does not significantly affect the $N(\mathrm{H\,I})_{\mathrm{AGD}}$ distribution. The WF effect influences the optical depth and spin temperature in opposite ways, i.e., increases T_s and decreases τ. These quantities are the main ingredients of $N(\mathrm{H\,I})_{\mathrm{AGD}}$ (c.f., Equation (16)), and therefore the two results of

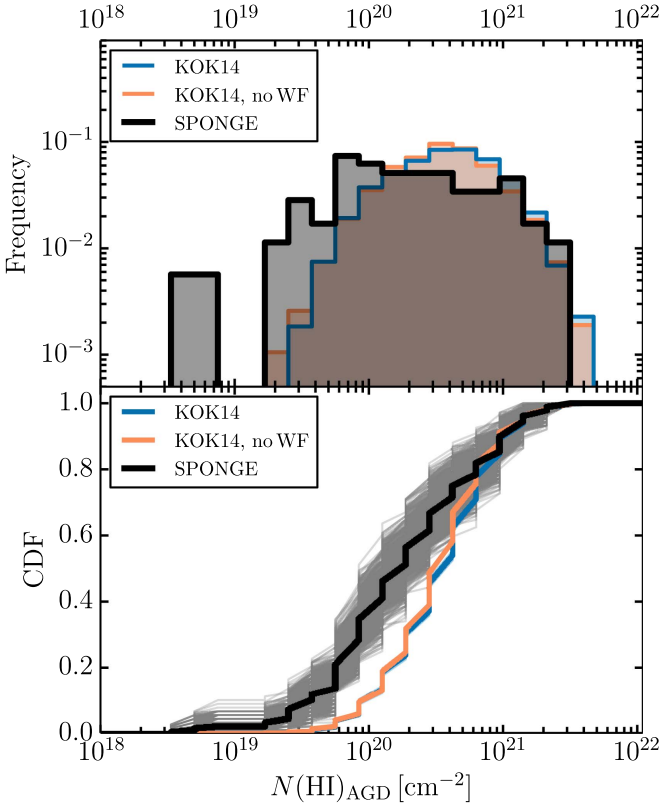

Figure 17. Top: histograms of $N(\mathrm{H\,I})_{\mathrm{AGD}}$ (Equation (16)) for all components which "match" between H I emission and absorption (Equations (9) and (10)) following the AGD analysis of 52 21-SPONGE H I spectral pairs (thick, solid black) and 9355 KOK14 H I spectral pairs with the WF effect (thin, solid blue) and without the WF effect (thin, solid orange). Bottom: CDFs of the same results, with 1000 bootstrapped samples drawn from the full sample with replacement (shown in lighter-shaded colors according to the legend) to illustrate the effect of sample size and outliers on the CDF.

the WF effect may cancel each other out when computing component-based column density. We conclude that the complexity of factors incorporated into the H I column density makes it a less useful tool for isolating the importance of the WF effect.

7. Summary and Conclusions

Detailed comparisons between observations and simulations are crucial for understanding the physics behind the observed properties of the ISM. Armed with synthetic 21 cm emission and absorption profile data created from the 3D hydrodynamical simulations from KOK14 and high-sensitivity H I observations from 21-SPONGE, we address two main questions: (1) how well do H I spectral lines and our analysis methods recover simulated properties of interstellar gas structures; and (2) how do simulated H I spectra compare with real observations? To analyze 9355 synthetic and 52 real observations in an unbiased and uniform way, we apply the AGD algorithm (Lindner et al. 2015) identically to both data sets. With these fits in hand, we compare simulated properties of gas structures along each LOS with observed properties of the Gaussian components.

We summarize the main results:

1. For gas structures defined by peaks in n/T_s along random LOSs in the KOK13 simulations, Gaussian fits by AGD to synthetic H I absorption lines are able to recover gas structures successfully (Figure 3). The recovery completeness (Equation (11)) is 99% for high-latitude LOSs ($|b| > 50°$), 67% for mid-latitude LOSs ($20 < |b| < 50°$), and 53% for low-latitude LOSs ($0 < |b| < 20°$). The completeness declines with decreasing latitude because the LOS complexity is highest at the lowest latitudes. When these structures are matched to spectral line components in both H I absorption and emission, the completeness is 83%, 38%, and 29% for high, mid, and low latitudes, respectively. The decline in recovery completeness when matches between gas structures and both H I absorption and emission components are required reflects the difficulty in associating unambiguous spectral features in the presence of line blending and turbulence.
2. We use AGD fits to synthetic lines and simple radiative transfer to compute observational estimates of spin temperature ($T_{s,\mathrm{AGD}}$) and column density ($N(\mathrm{H\,I})_{\mathrm{AGD}}$) for matched pairs of H I absorption and emission lines. We compare these estimates with the simulated spin temperatures ($T_{s,\mathrm{true}}$) and column densities ($N(\mathrm{H\,I})_{\mathrm{true}}$) of corresponding structures in the simulation. The observed and simulated spin temperatures agree within a factor of 2 for the majority of structures (68%; Figure 4). At high temperatures, $T_{s,\mathrm{AGD}}$ overestimates the $T_{s,\mathrm{true}}$ due to velocity offsets between H I absorption and emission lines caused by turbulent motions (Figure 5).

   The observed and simulated H I column densities also agree well for the majority of structures. However, the scatter is slightly larger than in the case of spin temperature, because $N(\mathrm{H\,I})_{\mathrm{AGD}}$ incorporates all uncertainty in $T_{s,\mathrm{AGD}}$ (Figure 6). Furthermore, the agreement between inferred and true properties declines at low Galactic latitude and for low-τ components, where LOS-blending components hinder clear associations between emission and absorption spectral lines (Figure 7).

   Overall, the agreement between temperature and column densities inferred from synthetic spectra and computed from physical conditions in the simulation is encouraging. Future comparisons with next-generation simulations will allow us to construct "correction functions" for observed spin temperature and column density distributions.
3. We find more fitted absorption and emission lines per LOS (N_{AGD}) in the 21-SPONGE observations than the KOK14 synthetic observations (Table 1). This difference reflects the fact that the simulated scale heights of the CNM and WNM in the KOK13 simulations are lower than in observations, due to velocity dispersions lower than seen in observations ($\sim$5–7 km s^{-1}). These results are derived from identical implementation of AGD to 21-SPONGE and KOK14, and thus the comparison is unaffected by biases introduced by AGD analysis. The discrepancy reflects the limitations of local box simulations, with a simplified treatment of supernova feedback, in producing realistic synthetic spectral lines.

   In addition, there are comparatively fewer matches per LOS in 21-SPONGE than KOK14. The so-called mismatch in angular resolution between 21-SPONGE H I emission ($\sim$3.′5) and absorption (1–40″) complicates

the matching process described by Equations (9) and (10). In the future, we plan to quantify this effect and correct the observational results by smoothing simulated spectra.

4. Using AGD, we objectively compare the properties of spectral lines fitted by AGD to H I absorption from 21-SPONGE and KOK14. The 21-SPONGE spectra have a wider range in mean velocity (right panel, Figure 10), due to the limited horizontal box size of the simulation. Furthermore, at high Galactic latitudes where the influence of the global effect is weakest, $N_{\rm AGD}$ and matching statistics agree between 21-SPONGE and KOK14. This indicates that simulated Galactic rotation plays an important role in observed H I properties, and improved implementations of global effects will improve the completeness statistics of H I structure recovery, and improve the completeness characterization discussed in Summary points 1, 2, and 3.
5. We find that KOK14 spectra include more low-τ and high-Δv absorption lines than are seen in 21-SPONGE (Figures 10 and 11), despite being well above the 21-SPONGE sensitivity and resolution limits. These broad spectral lines are often found without narrower, blended lines, which is a profile not seen in observations by 21-SPONGE or previous H I absorption line surveys (e.g., HT03, Roy et al. 2013). These are likely the result of the absence of a hot, large filling-factor gas phase in the KOK13 simulations (which would increase the number of LOSs without detectably absorbing neutral gas), or possibly some aspect of the simple treatment of the WF effect. In particular, we find that excluding the WF effect enhances the population of these discrepant H I absorption components, and suggests that the WF effect is important for realistic spectral line properties. These features are not obvious in comparisons of integrated or per-channel properties, and reflect the utility of studying velocity-resolved spectral components.
6. We find that H I absorption spectra are more useful probes of ISM physics in comparison with simulations than H I emission spectra. Properties of components fitted to H I emission profiles are affected by angular resolution mismatch and stray radiation, and are not sensitive to the implementation of the WF effect.
7. The AGD-derived spin temperature from KOK14 has more high-temperature gas ($1000 < T_{s,\rm AGD} < 4000$ K) relative to 21-SPONGE. The AGD method is not biased against high temperatures, and the 21-SPONGE observations have sufficient sensitivity for detecting gas at similar values. In KOK14, the highest-temperature components have large line widths and low optical depths, which is a type of profile not seen in 21-SPONGE (Figure 15). We conclude that the lack of observed components with $T_s > 1000$ K is not affected by sensitivity or the analysis method. We suggest that this gas may have even higher temperatures ($T_s \sim 7000$ K) than what 21-SPONGE is sensitive to and than what the KOK14 implementation of the WF effect allows (i.e., $1000 < T_s < 4000$ K). Again, future work is required to understand the importance of the WF effect in more detail. It is also important to test whether more realistic treatment of star formation feedback, including a hot ISM (see Kim & Ostriker 2016), reduces the incidence of features with $T_{s,\rm AGD} \sim$ 1000–4000 K in simulations.

Overall, we are encouraged that the AGD analysis and radiative transfer method presented here is a useful tool for diagnosing important physical conditions within ISM simulations. In the future, we will apply the strategies described here to updated simulations in order to derive correction functions for observational biases in real H I data. Upcoming large H I absorption surveys such as GASKAP at the ASKAP telescope (Dickey et al. 2013) will contribute many more sources and improve the observational statistics. The objective and efficient nature of the AGD analysis strategy presented here is well-suited for future large observed and simulated data sets, and will be important for understanding the balance of CNM and WNM in the local and extragalactic ISM.

This work was supported by the National Science Foundation (NSF) Early Career Development (CAREER) Award AST-1056780. C.E.M. acknowledges support by the NSF Graduate Research Fellowship and the Wisconsin Space Grant Institution. S.S. thanks the Research Corporation for Science Advancement for their support. The work of E.C.O. and C.-G. K. was supported by NSF grant AST-1312006. The National Radio Astronomy Observatory is a facility of the NSF operated under cooperative agreement by Associated Universities, Inc. The Arecibo Observatory is operated by SRI International under a cooperative agreement with the NSF (AST-1100968), and in alliance with Ana G Méndez-Universidad Metropolitana, and the Universities Space Research Association.

Appendix

To test for the effect of stray radiation on H I emission spectra, we analyze data from the LAB survey (Kalberla et al. 2005). The LAB spectra were measured with a $\sim 35'$ beam, whose shape was carefully modeled in order to remove contamination from stray radiation. We apply the AGD algorithm in the same manner as described in Section 6.3 to LAB spectra in the direction of the 52 21-SPONGE sources. In Figure 18, we reproduce Figure 13 including the LAB decomposition in red.

From Figure 18, the LAB $\Delta v_{0,\rm em}$ distribution is shifted to larger values relative to KOK14 and 21-SPONGE. As a result of the much larger angular resolution of the LAB survey, the AGD decomposition of LAB data in Figure 18 features fewer narrow velocity components ($\Delta v_{0,\rm em} < 2$ km s^{-1}), likely because the H I emission is smoothed over larger angular scales than in the 21-SPONGE spectra (from Arecibo Observatory, with $\sim 3\farcm5$ angular resolution).

Furthermore, the LAB decomposition contains large-line width ($\Delta v_{0,\rm em} > 30$ km s^{-1}), low-brightness temperature ($T_{B,0} < 1$ K) components similar to 21-SPONGE. However, there is a population of 21-SPONGE components with $\Delta v_{0,\rm em} \sim$ 50–100 km s^{-1} outside the LAB distribution. Given that stray radiation has been removed from the LAB spectra, this type of spectral feature may be indicative of stray radiation.

Future work is needed to understand and remove the stray radiation contamination from Arecibo spectra. Kalberla et al. (2010) found that stray radiation contributed up to 35% to some GASS H I spectra, however the effect is typically <10% and is not significant at Galactic latitudes below $\sim 60°$ (e.g., McClure-

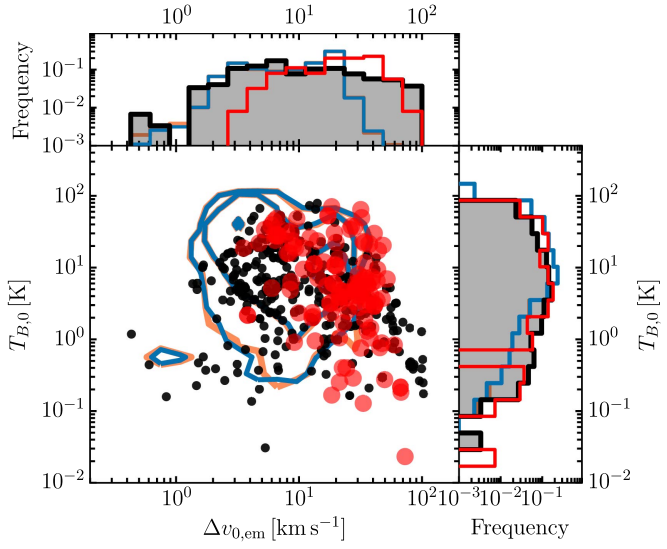

Figure 18. Parameters of Gaussian components ($\Delta v_{0,\mathrm{em}}$, $T_{B,0}$) fitted by AGD to H I emission spectra from 21-SPONGE (black) and KOK14 synthetic observations including the WF effect (blue) and without the WF effect (orange). Contours indicate the 1, 2, and 3σ limits for the KOK14 distribution. We also include the AGD decomposition of H I emission spectra in the direction of the 21-SPONGE sources from the LAB survey (Kalberla et al. 2005) in red.

Griffiths et al. 2009). In Murray et al. (2015), we compared 21-SPONGE emission spectra with the GALFA-H I (Peek et al. 2011) and LAB surveys (Kalberla et al. 2005) and concluded that differences are generally within 3σ uncertainties. In a future paper, we will compare the KOK14 synthetic H I emission spectra and data from the LAB and GALFA-HI surveys objectively using AGD in order to statistically quantify the effect of stray radiation on observational data.

References

Acreman, D. M., Dobbs, C. L., Brunt, C. M., & Douglas, K. A. 2012, MNRAS, 422, 241
Beaumont, C. N., Offner, S. S. R., Shetty, R., Glover, S. C. O., & Goodman, A. A. 2013, ApJ, 777, 173
Begum, A., Stanimirović, S., Goss, W. M., et al. 2010, ApJ, 725, 1779
Carilli, C. L., Dwarakanath, K. S., & Goss, W. M. 1998, ApJL, 502, L79
Chengalur, J. N., Kanekar, N., & Roy, N. 2013, MNRAS, 432, 3074
Crovisier, J., Kazes, I., & Aubry, D. 1978, A&AS, 32, 205
Dickey, J. M., & Lockman, F. J. 1990, ARA&A, 28, 215
Dickey, J. M., McClure-Griffiths, N., Gibson, S. J., et al. 2013, PASA, 30, e003
Dickey, J. M., McClure-Griffiths, N. M., Gaensler, B. M., & Green, A. J. 2003, ApJ, 585, 801
Douglas, K. A., Acreman, D. M., Dobbs, C. L., & Brunt, C. M. 2010, MNRAS, 407, 405
Draine, B. T. 2011, Physics of the Interstellar and Intergalactic Medium (Princeton, NJ: Princeton Univ. Press)
Duarte-Cabral, A., Acreman, D. M., Dobbs, C. L., et al. 2015, MNRAS, 447, 2144
Duarte-Cabral, A., & Dobbs, C. L. 2016, MNRAS, 458, 3667
Dwarakanath, K. S., Carilli, C. L., & Goss, W. M. 2002, ApJ, 567, 940
Falgarone, E., Lis, D. C., Phillips, T. G., et al. 1994, ApJ, 436, 728
Field, G. B. 1959, ApJ, 129, 536
Field, G. B., Goldsmith, D. W., & Habing, H. J. 1969, ApJL, 155, L149
Hartmann, D., & Burton, W. B. 1997, Atlas of Galactic Neutral Hydrogen (Cambridge: Cambridge Univ. Press)
Heiles, C., & Troland, T. H. 2003a, ApJS, 145, 329
Heiles, C., & Troland, T. H. 2003b, ApJ, 586, 1067
Hennebelle, P., Audit, E., & Miville-Deschênes, M.-A. 2007, A&A, 465, 445
Kalberla, P. M. W., Burton, W. B., Hartmann, D., et al. 2005, A&A, 440, 775
Kalberla, P. M. W., McClure-Griffiths, N. M., Pisano, D. J., et al. 2010, A&A, 521, A17
Kim, C.-G., & Ostriker, E. C. 2016, arXiv:1612.03918
Kim, C.-G., Ostriker, E. C., & Kim, W.-T. 2013, ApJ, 776, 1
Kim, C.-G., Ostriker, E. C., & Kim, W.-T. 2014, ApJ, 786, 64
Lazareff, B. 1975, A&A, 42, 25
Lindner, R. R., Vera-Ciro, C., Murray, C. E., et al. 2015, AJ, 149, 138
Liszt, H. 2001, A&A, 371, 698
McClure-Griffiths, N. M., Pisano, D. J., Calabretta, M. R., et al. 2009, ApJS, 181, 398
McClure-Griffiths, N. M., Green, J. A., Hill, A. S., et al. 2013, ApJL, 770, L4
McKee, C. F., & Ostriker, J. P. 1977, ApJ, 218, 148
Mebold, U., Winnberg, A., Kalberla, P. M. W., & Goss, W. M. 1982, A&A, 115, 223
Mohan, R., Dwarakanath, K. S., & Srinivasan, G. 2004, JApA, 25, 185
Murray, C. E., Lindner, R. R., Stanimirović, S., et al. 2014, ApJL, 781, L41
Murray, C. E., Stanimirović, S., Goss, W. M., et al. 2015, ApJ, 804, 89
Peek, J. E. G., Heiles, C., Douglas, K. A., et al. 2011, ApJS, 194, 20
Pettitt, A. R., Dobbs, C. L., Acreman, D. M., & Price, D. J. 2014, MNRAS, 444, 919
Roy, N., Kanekar, N., & Chengalur, J. N. 2013, MNRAS, 436, 2366
Saury, E., Miville-Deschênes, M.-A., Hennebelle, P., Audit, E., & Schmidt, W. 2014, A&A, 567, A16
Shetty, R., Glover, S. C., Dullemond, C. P., & Klessen, R. S. 2011, MNRAS, 412, 1686
Smith, R. J., Glover, S. C. O., Clark, P. C., Klessen, R. S., & Springel, V. 2014, MNRAS, 441, 1628
Stanimirović, S., & Heiles, C. 2005, ApJ, 631, 371
Stanimirović, S., Murray, C. E., Lee, M.-Y., Heiles, C., & Miller, J. 2014, ApJ, 793, 132
Wolfire, M. G., Hollenbach, D., McKee, C. F., Tielens, A. G. G. M., & Bakes, E. L. O. 1995, ApJ, 443, 152
Wolfire, M. G., McKee, C. F., Hollenbach, D., & Tielens, A. G. G. M. 2003, ApJ, 587, 278
Wouthuysen, S. A. 1952, AJ, 57, 31